POLITECNICO DI TORINO

DEPARTMENT OF APPLIED SCIENCE AND TECHNOLOGY

Doctorate in Electronic Devices

(XXVI ciclo)

ZnO nanowires for energy harvesting and gas sensing applications: a quantum mechanical study

Advisors:

Prof. Giancarlo Cicero

Prof. Alessandra Catellani

Candidate:

Kiptiemoi Korir Kiprono

Marzo 2014

In physics, you don't have to go around making trouble for yourself - nature does it for you.

Frank Wilczek

Contents

Dedicated to my parents

List of Figures

List of Tables

Chapter 1

Introduction

Ab initio total-energy calculations based on electronic structure theory have proved to be a predictive tool to study the properties of materials, in the field of both basic and applied research. The enormous increase in computational power has allowed to perform calculations with high accuracy, and on increasing length and time scales, which renders feasible the study of 'real' systems. On the other hand, a significant new development in experimental techniques and material preparation makes it possible to probe structure of matter in ways never realized before. One of the best examples are nanostructures of ZnO, where theoretical predictions have stimulated experiments and led to a deeper understanding of the nature of such systems.

The theoretical approach, which is by far the most used at the present time for the calculation of the total energy and other ground state properties of matter, is the Density Functional method (DFT), which was first developed by Hohenberg, Kohn and Sham. These authors demonstrated that the exact ground state energy of the many-body quantum-mechanical system is a unique functional of its charge density. Based on this statement they built a method to map the many-body problem into a single particle one, mimicking the interactions with an effective potential containing all the many-body effects. This approach allowed to describe the state of matter in terms of its equilibrium structure, its average electronic charge density, its total energy, and so forth.

In the present work, we applied the ab initio DFT approach to investigate the response of ZnO nanaowires to specific external perturbations, in order to describe some transductive and sensing applications. To this aim, piezoelectricity and gas (ethanol) sensing mechanisms are considered, along with the role of oxygen vacancies, and hydrogen incorporation, as possible causes of intrinsic n-doping, to parallel the experimental results.

ZnO is one of the most important multi-functional semiconductors that possess many properties of technological relevance [8]. Indeed, the realization of p-type doping in ZnO

[9], as well as fabrication of flexible transparent thin film transistor [10] that are expected to meet emerging technological demands where silicon cannot provide a solution. Therefore, this imply that wide-gap metal oxides, such as ZnO have the potential of becoming future electronic material of choice. Recent advances in growth techniques have resulted in fabrication of one-dimensional nanostructures in the form of nanowires, nanobelts and nanorods [11, 12], which have attracted attention because of their unique and novel applications in optics, optoelectronics, catalysis, and piezoelectricity. [13].
In particular, ZnO nanowires (NWs) are envisaged as ideal candidate for energy harvesting application i.e., fabrication of nano-generators where piezoelectricity is employed to convert mechanical energy to electrical energy for the operation of low-power electronics [14]. Piezoelectric response of a material is usually expressed in terms of effective piezoelectric coefficient, which can be obtained both experimental and theoretical approach. In terms of experimental results, as pointed out in Ref. [15], several artifacts dominate these measurements resulting in scatter in and conflicting results trends in the reported size effects. These artifacts are related to uncertainties in boundary conditions, metrology of the cross-section, instrument calibration and sample manipulation [16].
In ab initio studies, effective piezoelectric coefficient is determined within modern theory of polarization proposed by Resta and co-workers [17], where the rate change in polarization is normalized to volume. Therefore, this approach works well only for systems whose volume is well defined, e.g. bulk. However, in NWs this approach becomes unreliable as shown by the large spread in values reported in literature [18–20]; therefore, the role of size effect in this context need to be investigated further.
Semiconductor gas sensors have been extensively investigated for practical applications such as the detection of gas leaks and the environmental monitoring of gaseous pollutants [21]. Since the earliest reports in this field, research efforts were focussed on improving gas response, selectivity, and sensor stability [22, 23]. The ability to detect ethanol gas is highly desirable as it is used in a variety of commercial products and industrial processes. Ethanol sensors based on ZnO nanostructures have been demonstrated by a number of groups [4, 24–26]. The exact mechanism that determines gas response is still not well understood; however, it is generally agreed that metal oxide based gas sensors rely on changes in electrical conductivity upon interaction with the surrounding atmosphere: when operating within semiconducting temperature range, surface reactions determine the device conductivity. Therefore, for their practical use in sensing application, further innovations are still in demand to address open questions.
Controlling the surface chemistry and conductivity of ZnO remains a major challenge. Even relatively small concentrations of native point defects and impurities (down to 10^{-14}cm^{-3} or 0.01 ppm) can significantly affect the electrical, optical and sensing properties of semiconductors [27]. Therefore, understanding the role of native point defects (i.e. vacancies, interstitials, and antisites) and the incorporation of impurities is key

toward controlling properties of ZnO. Although a number of studies have reviewed the nature and the thermodynamics of intrinsic point defects in ZnO [28, 29], the understanding is still incomplete. In particular, the role of oxygen vacancies has been insufficiently analyzed, for example, the distribution and concentration of oxygen vacancies on the surface and surface region of ZnO nanostructures is still not well understood. Vlasenko *et al.* [30] reported noticeable concentration of oxygen vacancies in as-grown ZnO only after electron irradiation, while Selim *et al.* [31] on the other hand found high concentration in as grown ZnO detectable even without need of irradiation, to quote only a few. Similar inconsistencies have been reported also in theoretical work [32–34].

In the present work, we applied the ab initio DFT approach to investigate the response of ZnO nanaowires to specific external perturbations, in order to describe some transductive and sensing applications. To this aim, piezoelectricity and gas (ethanol) sensing mechanisms are considered, along with the role of oxygen vacancies, and hydrogen incorporation, as possible causes of intrinsic n-doping, to parallel the experimental results. An approach based on Wannier Function (WFs) is used to study piezoelectric properties of ZnO NWs and the problem associated with ill-definition of volume in nanostructure is overcome. A scheme that passes through normalization in terms of number of formula units per supercell (a ZnO pair in the case of zinc oxide nanosystems) without loss of generality is proposed. This approach takes advantage of the WFs definition that allows to calculate local dipole contributions (one for each ZnO couple) to the average dipole of a system. In this way, it is shown that the piezoelectric properties of NWs are only mildly influenced by size reduction to the nanoscale. On the other hand, the effective strain energy decreases with decreasing the size of the NWs, and for the smallest wire it is reduced by about 50 %, thus making them ideal candidates for building efficient energy scavenging devices irrespective of the fact that NW based nanogenerators (with typical size of 40 nm) are expected to have piezoelectric properties similar to bulk ones. Concerning the intrinsic n-character of the samples, our study reveals that the presence of hydrogen modifies the electrical properties of ZnO, particularly their conductivity, which is attributed to the fact that hydrogen acts as a donor thus populate electrons to the conduction band. Ethanol gas sensing on ZnO is mediated by competitive adsorption between pre-adsorbed oxygen molecules and ethanol on the surface. In particular, it is shown that due to ethanol large adsorption energy when compared to that of oxygen, ethanol molecules are able to remove oxygen from the surface resulting in improved surface conductivity. Furthermore, it is revealed that increase in surface conductivity is solely due to release of trapped electrons to conduction band (CB), instead of a direct injection to CB as claimed in previous studies. At surfaces, conductance switching can be achieved solely by surface chemistry i.e., adsorption and desorption of gas molecules, thus this open the possibility of developing sensors with improved performance.

Finally, it is shown that oxygen vacancies are formed on the surfaces of ZnO in ambient

condition: if they occur in deeper layers they tend to diffuse to the surface. Our unified study predicts that non-destructive introduction of oxygen vacancies on the surface of ZnO can be achieved by using SO as one of the precursors during growth because it induces a Zn rich environment, which is ideal for formation of oxygen vacancies.
This dissertation is organized as follows. In the first chapter a general description of open questions associated with ZnO nanostructures applications in energy scavenging and gas sensing, and the approaches used to address these problems are presented. Chapter 2 discusses aspects that renders ZnO nanostructures a superior material for energy harvesting and gas sensing. Chapter 3 and 4 are centered on the computational methodology that has been applied to investigate ZnO nanostructures. First the fundamental theory of ab initio DFT and the various extensions used in this work are introduced, then the optimization of the computational parameters is discussed. In Chapter 5 the results on the simulation of piezoelectric properties of ZnO NWs is presented, while Chapter 6 is dedicated to studies on ethanol gas sensing mechanism. Analysis on formation and diffusion mechanism of oxygen vacancies near surface regions of ZnO are presented in Chapter 7.

Chapter 2

ZnO nanowire applications

Recently, zinc oxide (ZnO) has attracted much attention within the scientific community due to its wide range of potential applications that has been attributed to its unique electrical, piezoelectric, optoelectronic, and photochemical properties. The renewed interest in this material has been prompted by the development of growth technologies for the fabrication of high quality single crystals and epitaxial layers, allowing for the realization of ZnO-based electronic and optoelectronic devices. ZnO has a direct and wide band gap of about 3.4 eV and a large free-exciton binding energy (∼60 meV) such that excitonic emission processes can persist at or even above room temperature [8, 35]. At ambient pressure and temperature, ZnO crystallizes in the wurtzite (B4 type) structure, as shown in Fig. 2.1. This is a hexagonal lattice, belonging to the space group P63mc, and it is characterized by two interconnecting sublattices of Zn^{2+} and O^{2-}, such that each Zn ion is surrounded by a tetrahedra of O ions, and vice-versa. This tetrahedral coordination gives rise to polar symmetry along the hexagonal axis (c axis in Fig. 2.1), which is responsible for a number of the properties of ZnO, including its piezoelectricity and spontaneous polarization. The most important physical properties

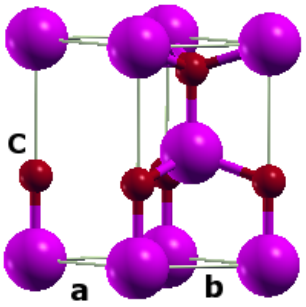

FIGURE 2.1: Ball and stick representation of the hexagonal wurtzite structure of ZnO. Zn atoms are represented as large purple spheres, while O atoms are shown as small red spheres. One unit cell is outlined for clarity.

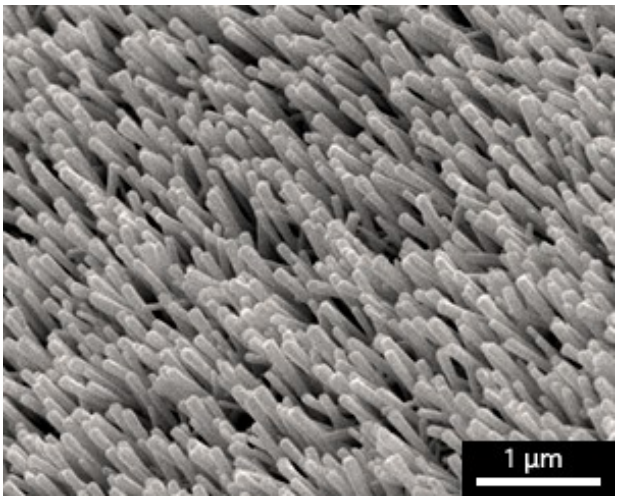

FIGURE 2.2: Scanning electron microscopy image of ZnO nanowires grown on paper substrate using chemical solution [1].

of ZnO are presented in table 5.2.

Property	value
Lattice parameter	a = b = 3.2496 Å
	c = 5.2042 Å
	u = 0.3819 Å
Band gap	3.3 eV (direct)
Melting point	2248 K
Density	5.606 g/cm^3
Hardness (Moh's scale)	4.5

TABLE 2.1: Physical properties of bulk wurtzite ZnO [7].

Most recently, there has been a significant shift in interest towards ZnO nanostructures due to their unique physical, chemical, and electronic properties, which make them ideal candidates for a wide range of technological applications [4, 36–38].

Owing to their remarkable properties coupled with the need for device miniaturization, large effort has been focused on the synthesis, characterization and device applications of ZnO nanomaterials. A large variety of ZnO nanostructures, such as nanowires, nanotubes, nanorings, and nano-tetrapods have been successfully grown via a variety of methods including chemical vapor deposition, thermal evaporation, and electrodeposition [39–41] on many different substrate. For example, in the case of ZnO nanowires (NWs), it has been demonstrated that they can be even grown on many different kind of hard and flexible by chemical solution. Fig. 2.2 shows for example a ZnO NWs sample grown on paper [1]. It is worth noting that as the dimension of semiconductor materials continuously shrinks down to nanometer or even smaller scale, some of their properties undergo changes with respect to the bulk phase know as quantum size effects. Although

these effects have been extensively studied when considering optical, electrical or mechanical properties, it is less know how size affects other properties. For example, in the case of piezoelectric materials, such as ZnO, it is not know how size affects spontaneous polarization or piezoelectricity, although different applications rely on these properties.

2.1 ZnO NWs for mechanical energy harvesting

The global energy consumption is projected to rise by more than 56 % by 2040 [42]. Assuming that current energy policies and practices remain in place, most of the increased energy production is expected to come from combustion of fuels, such as oil, ethanol, natural gas and coal. Therefore, a commensurate increase in CO_2, which is a prominent green-house gas anticipated, and much of which is attributed to burning coal, which is becoming the fastest growing source of energy globally. To moderate global reliance on exhaustible natural resources and their environmentally hazardous combustion, more scientific efforts have been directed toward reducing the cost of energy production from renewable sources. There exist many potential renewable energy technologies in the form of solid-state devices, such as, piezoelectric nanogenerators, which convert mechanical energy (such as body movement like muscle stretching), vibrational energy (such as acoustic) and hydraulic energy (such as body fluid and blood flow) into electric energy that can be used to power nanodevices that operate at a very low power, i.e. in the range from nW to μW [15].

Piezoelectricity is a linear electromechanical coupling, which manifests itself as a direct effect $\mathrm{P}_i = \mathrm{d}_{ijk}\sigma_{jk}$, where P is the polarization vector, σ is the stress tensor, and d is the piezoelectric third rank tensor. In direct piezoelectricity, application of mechanical stress to a piezoelectric material results in generation of electrical charges (voltage) on its surface. This charge can be utilized in a variety of applications, such as, sensing and energy harvesting.

The first piezoelectric nanogenerator was developed by Wang *et. al* [14] and it was based on ZnO NWs. The mechanism of power generation in such devices relies on the coupling between the semiconducting and piezoelectric properties of the material. Moreover the power generated with these devices depends on the direction of the exerted force i.e., perpendicular or parallel to the axis of the NW, and can lead to production of alternating or direct current, respectively, as illustrated in Fig. 2.3 and Fig. 2.4.

When piezoelectric semiconducting NWs are subjected to an external force, a piezoelectric potential is generated in the nanowire, due to the relative displacement of the cations with respect to the anions. The piezoelectric potential in the nanowires originates a displacement electrical current in the external circuit if a Shottky barrier is present between the ZnO NWs and the electrodes. A DC-type output originates when a force is applied

on a flexible top electrode, see Fig. 2.3. In this case the NWs beneath are subjected to forces with different directions, hence lateral bending occurs, and electrons flow from the compressed side of the NW to the top electrode (for more details see Ref. [43]). AC-type current occurs when ZnO NWs are compressed by an external force, directed along the NW axis (c-axis) as shown in Fig. 2.4. In this case, a piezoelectric potential is generated NW along the NW axis, therefore, one side of the NW experiences a negative piezoelectric potential and the other side a positive potential. The piezo-potential moves electrons in the external circuit accumulating them at the interface between the electrode at positive potential and the of the NWs (Fig. 2.4). As the external force is removed and the compressive strain is released, the piezoelectric potential disappears inside the NW and the accumulated electron flow back via the external circuit, creating a negative electric pulse, and consequently an AC signal is generated.
During the first experiments conducted by Wang et al. [14], nano generators were driven by a force that induce lateral bending of ZnO NWs i.e., using atomic force microscope (AFM) tip scanning or ultrasonic vibrations. Wang et al. [14] established that in lateral

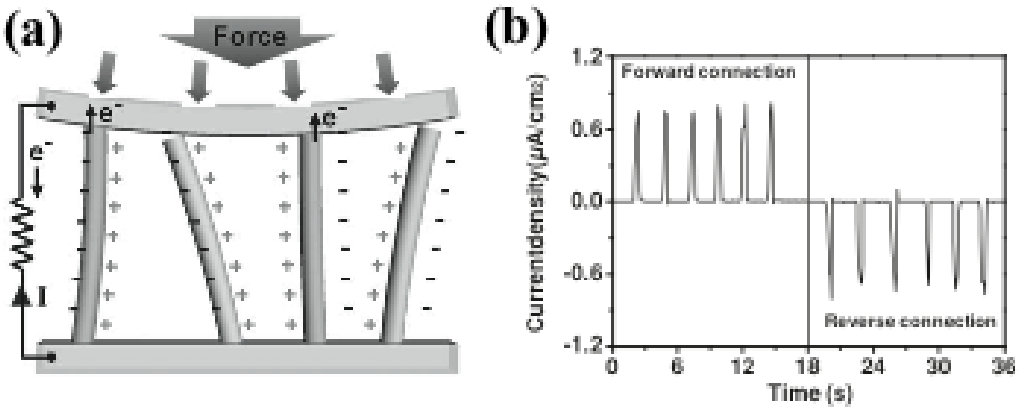

FIGURE 2.3: (a) Schematic diagrams showing DC-type output charge generation from ZnO NWs. ZnO NWs are brought into contact with the top ITO electrode by applying an external force, electrons flow from the compressed sides of the ZnO nanorods to the top electrode, (b) DC-type charge generation profile (Ref. [2]).

bending by an AFM tip, the maximum potential produced at the NW surface has an inverse relationship with the cube of its length/diameter, and a direct relationship with the lateral displacement by the probe. Furthermore, it was shown that for a ZnO NW with a diameter of 50 nm and length of 600 nm, the piezoelectric voltage is in the order of 0.3 V, which is enough to drive metal-semiconductor Schottky diode at the interface of the AFM probe and the NW.
Since the first experiment by Wang and coworkers [14], there have been sustained efforts to improve the design and fabrication of nanogenerator capable of harvesting various

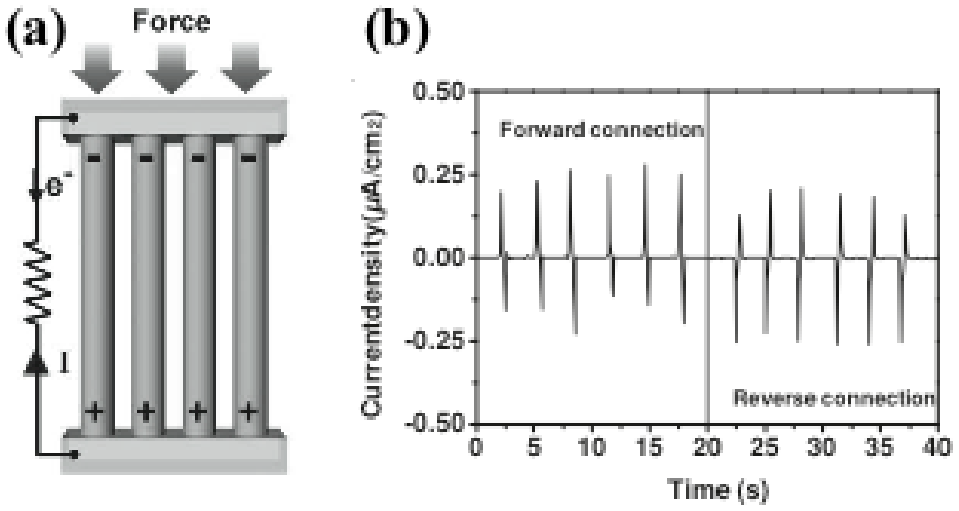

FIGURE 2.4: (a) Schematic diagrams showing output charge generation from ZnO nanowire. The electrons flow from the electrode in contact with the sides of the nanowire having a negative potential to the opposite electrode in contact with the sides of the nanowire having a positive potential through the external circuit under a compressive force, (b) AC-type charge generation (forward and reverse connections) (Ref. [2]).

sources of mechanical energy with better performance [15]. This resulted in the development of a fiber-based flexible nanogenerator with ZnO NWs [44], an integrated transparent flexible nanogenerator with ZnO nanorods [43], an integrated sound-driven nanogenerator with ZnO NWs [45], and a flexible high-output nanogenerator based on lateral ZnO nanowire arrays with output voltages of up to 2.03 V and a peak power density of 11 mW cm^3, which was used successfully to light up a commercial light-emitting diode [46], as shown in Fig. 2.5 .

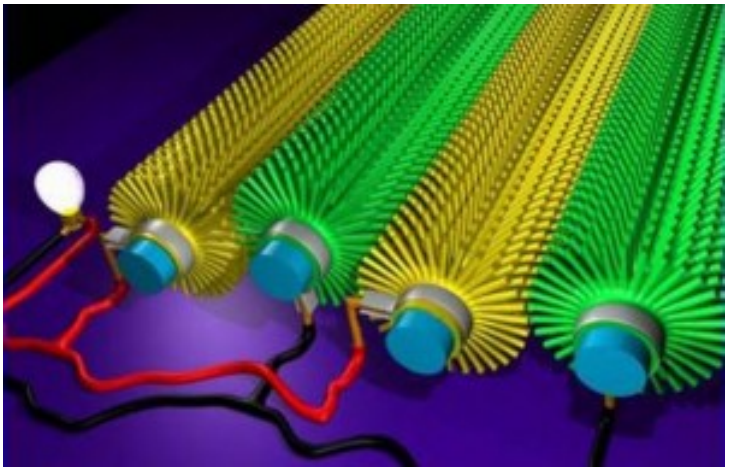

FIGURE 2.5: A schematic illustration of the microfiber-nanowire hybrid nanogenerator, which is the basis of using fabrics for generating electricity [3].

On the theoretical side, a large effort has been devoted to investigating how the piezoelectric properties of a material, and specifically ZnO, changes when small diameter nanowires are considered. One of the main question to be addressed is whether confinement effects can also be observed in the piezoelectric behavior of nano-sized system. Espinosa and co-workers [19] studied the size-dependence of piezoelectricity in GaN and ZnO NWs with diameters ranging from 0.6 to 2.4 *nm* using the Berry-phase approach [47] implemented within DFT. A giant piezoelectric size effect was observed for both classes NWs, with GaN exhibiting larger and more extended size dependence than ZnO. Approximately two orders of magnitude enhancement in piezoelectric coefficient was demonstrated when the diameter of a nanowire is reduced to less than 1 nm.
On the contrary, mild enhancement of piezoelectric constants were identified for [0001] ZnO NWs, using similar DFT approach for NWs with diameter upto 2.8 nm [18]. The overview of piezoelectric trends of ZnO NWs presented in this section reinforces the fact that further characterization are needed to reduce the existing scatter and identify size-effects trends in the piezoelectricity of NWs. Coupling of improved experimental techniques that allow in-situ structural characterization and advanced computational methods would be needed to achieve a unified set of piezoelectric constant values and deeper understanding of the physics behind the observed effects.

2.2 ZnO NWs for gas sensing

During the last decade of 20^{th} century, there has been a strong interest in the development of wide bandgap semiconductor gas sensors for the detection of several molecules such as ethanol, liquified petroleum gas, CO_2 and CO. Gas sensors based on metal oxide semiconductor like SnO_2, TiO_2, WO_3, ZnO, Fe_2O_3, and In_2O_3 have an important role in environmental monitoring, chemical process controlling, personal safety, wine quality monitoring, and traffic safety [4, 26, 48]. These group of metal oxide are capable of operating at much higher temperatures than more conventional semiconductors such as silicon, thus they are suitable for sensing in extreme environment [35]. In particular, ZnO has a long history for use as a gas sensing material [49, 50], due to its low cost, easy production, compact size and simple measuring electronics [51].
Since the first demonstration of the ability of metal oxide nanowires to detect a variety of chemical species [52], the interest in this research area has grown exponentially in the past few years as testified by recent literature (see the following reviews [21, 23, 53–55]). Metal oxide nanostructures have several advantages with respect to traditional thin- and thick film sensors such as

- better sensitivity due to large surface-to-volume ratio
- superior stability owing to the high crystallinity [56]
- relatively simple preparation methods that allow large-scale production [53]
- ease to functionalize their surface with a target-specific receptor species [57] to achieve better selectivity
- possibility to achieve field-effect transistors (FET) configuration that allows the use of gate potential controlling the sensitivity and selectivity [58].

Gas sensors based on metal oxide nanostructures generally consist of three parts, i.e., the sensing element, the electrodes and a heater. Metal oxide nanostructures, often in the form of wire, are the active element that change their resistance upon exposure to target gases. The electrodes are used to measure the resistance of the sensing wires. Finally, the gas sensors are usually furnished with a heater so to achieve the working temperature that maximize the device response.

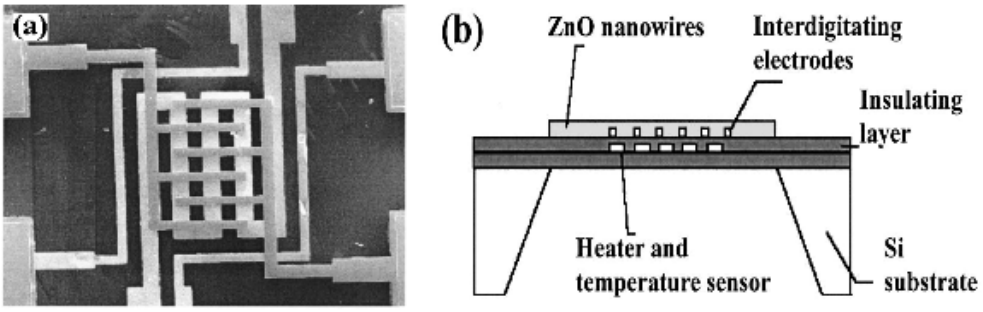

FIGURE 2.6: (a) Top-view SEM image of the fabricated substrate embedded with Pt interdigitating electrodes and Pt heater, (b) 3D schematic of the fabricated sensor structures (Ref. [4]).

In the example of Fig. 2.6 a ZnO NW based gas sensor has been fabricated on a silicon-based membrane embedded with Pt interdigitating electrodes and a heater [4]; the size of the membrane is 1.4×1.4 mm^2 and the device is 3×3 mm^2 in area, therefore reduced power consumption is achieved.

In particular in this study, we focus on the detection of ethanol because it is widely used in industries and in our daily life. For example, an ethanol sensor is contained in breath analyzers which are used to monitor ethanol vapour in human breath; this is correlated with ethanol concentration in the blood [59] and has help in reducing road fatalities related to drunken driving.

Various studies have demonstrated ethanol gas sensing capabilities of ZnO NWs [4, 60, 61]. Furthermore, these studies have shown that enhanced selectivity and sensitivity can be attained in ZnO nanostructures by doping or surface functionalization. For example, Kim and Son [62] showed that ZnO nanowires doped with 3% Al gave the highest sensitivity towards ethanol gas.

Yet the mechanism responsible for realization of ethanol gas sensing in ZnO is still not well understood. It is believed that ethanol adsorption/desorption on ZnO surface is responsible for changes in the electrical properties of the NW. However, it is less known how the presence of other gases in ambient condition affects sensitivity. Ethanol gas sensing mechanism is often explained based on complex experimental measurements, where several parameters are varied simultaneously hence it is difficult to understand the role of each parameter. Therefore, it becomes necessity to perform theoretical studies oriented to understanding the fundamentals of gas-sensing effects. Moreover, the effect of surface defects is also unclear for such a reaction. While it has been shown that surface oxygen vacancies on ZnO surfaces and nanostructures can enhance the adsorption strength of small molecules, including NO_2, NO, O_2, NH_3, H_2, H_2S (see for example Refs [63–65]) and even lead to dissociation of the adsorbate (NO_2, O_2) to fill the defect site [64, 66, 67], it is unclear whether the same effect occurs for ethanol.

Ab initio or quantum mechanical type calculations, in particular, have been used to investigate a wide variety of materials, their properties and their interactions with atoms and molecules. Such methods have proved extremely useful for examining gas/surface interactions due to their ability to model the direction of the charge transfer, the reaction mechanism, the structural changes and the electronic and magnetic properties involved. In order to take advantage of the benefits of a computational approach to studying these systems, reaction of alcohol molecules on ZnO NW surface needs to be investigated in a more realistic setting that may contribute to better understanding of real system i.e., by considering possible sources of n-type doping in ZnO, amongst others. Such studies are need in order build a more complete picture of gas-sensor surface reaction details, which will assist in determining the applicability of these materials for sensing in a wide range of environments.

Chapter 3

Methods

In the last decades, *ab initio* atomistic approach has emerged as a powerful tool able to predict material properties starting from a quantum description of the electrons. Among the possible methods proposed to solve the Schrödinger equation of a complex many-body system, the Density Functional Theory (DFT) is one of the most employed. In this chapter, the principles on which DFT is based are recalled and few practical aspect of DFT implementation in the case of periodic structures are presented.

3.1 The Born-Oppenheimer approximation

The DFT approach relies upon two basic assumptions: ions are regarded as classical particles and the adiabatic (Born-Oppenheimer) approximation holds, i.e. system for which a separation between classical motion of ions and quantum motion of electrons can be achieved. For such systems, the interaction potential among the ions $V(\{\mathbf{R}_A\})$ can be derived from first principles from equation:

$$V(\{\mathbf{R}_A\}) =< \psi_0|H(\{\mathbf{R}_A\})|\psi_0 > \tag{3.1}$$

Here H is the Hamiltonian of the system at a fixed atomic positions ($\{\mathbf{R}_A\}$) and ψ_0 is the corresponding ground state eigenfunction.
If we suppose to have a system composed by M ions and N electrons; then, the form of the Hamiltonian written in equation (3.1) would be:

$$H = -\sum_{i=1}^{N}\frac{1}{2}\nabla_i^2 - \sum_{A=1}^{M}\frac{1}{2M_A}\nabla_A^2 - \sum_{i=1}^{N}\sum_{A=1}^{M}\frac{Z_A}{\mathbf{r}_{iA}} + \sum_{i=1}^{N}\sum_{j>i}^{N}\frac{1}{\mathbf{r}_{ij}} + \sum_{A=1}^{M}\sum_{B>A}^{M}\frac{Z_A Z_B}{\mathbf{R}_{AB}} \tag{3.2}$$

(atomic units are used throughout).

The Born-Oppenheimer approximation is based on the observation that ions are much heavier than electrons so they move more slowly: the significant electronic velocities are, for electrons at Fermi level, 10^8 cm/sec while typical ionic velocities are at most 10^5 cm/sec. We therefore can consider the electrons to be moving in the field of fixed ions. Within this approximation, the second term of equation (3.2), the kinetic energy of the nuclei, can be neglected and the last term of (3.2), the repulsion between the nuclei, can be considered to be constant. Since any constant added to an operator simply shifts the operator eigenvalues without changing its eigenfunctions, we can remove it, so in equation (3.2) what remains is only the electronic Hamiltonian describing the motion of N electrons in the field of M fixed point charges located at r_{iA}

$$H_{elec} = -\sum_{i=1}^{N} \frac{1}{2}\nabla_i^2 - \sum_{i=1}^{N}\sum_{A=1}^{M} \frac{Z_A}{\mathbf{r}_{iA}} + \sum_{i=1}^{N}\sum_{j>i}^{N} \frac{1}{\mathbf{r}_{ij}} \tag{3.3}$$

The solution of a Schrödinger equation involving the electronic Hamiltonian

$$H_{elec}\psi_{elec} = E_{elec}\psi_{elec} \tag{3.4}$$

is the electronic wave function

$$\psi_{elec} = \psi_{elec}(\{\mathbf{r}_i\}; \{\mathbf{R}_A\}) \equiv \psi_R \tag{3.5}$$

which describes the motion of the electrons and explicitly depends on the electronic coordinates, but depends parametrically on the nuclear coordinates, as does the electronic energy:

$$E_{elec} = E_{elec}(\{\mathbf{R}_A\}) \tag{3.6}$$

The parametric dependence means that, for different arrangements of the nuclei, ψ_R is a different function of the electronic coordinates, but the nuclear coordinates do not appear explicitly in it. The total energy for a fixed nuclei configuration must also include the constant nuclear repulsion:

$$E_{tot} = E_{elec} + \sum_{A=1}^{M}\sum_{B>A}^{M} \frac{Z_A Z_B}{\mathbf{R}_{AB}} \tag{3.7}$$

3.2 Density Functional Theory

Density Functional Theory (DFT) is a mean-field approach to describe a system of many interacting electrons that was formulated in the sixties by Hohenberg and Kohn [68] and Kohn and Sham [69]. It is a theory for the electronic structure formulated in terms of

the electron density as basic unknown, instead of the electronic wavefunction. Since the density of particles in the ground state plays a central role in the theory, it can be considered as a "basic variable" and all properties of the system can be considered to be unique functionals of the ground state density. DFT can be regarded as the direct descendant of the Thomas-Fermi theory (1927) [70, 71]. Although Thomas-Fermi approximation is not accurate the approch illustrates the way DFT works. In the Thomas-Fermi method the kinetic energy of the system of electrons is approximated as an explicit functional of the density, idealized as non-interacting electrons in a homogeneous gas with density equal to the local density at any given point. Dirac improved this model and formulated the local approximation for exchange that is still in use today [72]. In this section the basic formalism of the theory is presented starting from the fundamental Hohenberg and Kohn theorems which demonstrate the central role played by the electron density in quantum mechanics.

3.2.1 Hohenberg-Kohn theorems

Let's consider a system of N electrons enclosed in a large box and moving under the influence of some time-independent local external potential $v(\mathbf{r})$. The first Hohenberg-Kohn theorem demonstrates that, for a system with a fixed number of particles, $v(\mathbf{r})$ is determined within an additive constant, once the electron density $n(\mathbf{r})$ is known. This means that the density determines univocally the external potential, and consequently the Hamiltonian and all the electronic properties of the system. According to this statement, the ground state expectation value of any observable (e.g. the Hamiltonian) is a unique functional of the ground state density n_0. In this formalism the total energy can be written as:

$$E_v[n] = \int n(\mathbf{r})v(\mathbf{r})d\mathbf{r} + F[n] \tag{3.8}$$

The functional $F[n]$ is a universal functional, sum of the kinetic and electron-electron repulsion energy and it is unique in the sense that it does not depend on the external potential which acts on the system. The second Hohenberg-Kohn theorem states that for any trial density $\tilde{n}$:

$$E_0 \leq E[\tilde{n}] \tag{3.9}$$

being E_0 the total energy calculated with respect to the exact ground state density n_0. The proof is based on the variational principle as for any trial wave function $\tilde{\psi}$:

$$< \tilde{\psi}|H|\tilde{\psi} >= \int \tilde{n}(\mathbf{r})v(\mathbf{r})d(\mathbf{r}) + F[\tilde{n}] = E_v[\tilde{n}] \geq E_v[n] \tag{3.10}$$

Equality stands only in the true ground-state. The variation of the total energy at constant number of electrons (N)

$$\delta \left\{ E_v[n] - \mu \left[\int n(\mathbf{r}) d(\mathbf{r}) - N \right] \right\} = 0 \tag{3.11}$$

leads to the Euler equation:

$$\mu = \frac{\delta E_v[n]}{\delta n} = v(\mathbf{r}) + \frac{\delta F_{HK}[n]}{\delta n} \tag{3.12}$$

where the Lagrange multiplier μ is the chemical potential.
By knowing the analytical expression for the energy functional, $E_v[n]$, and solving the Euler equation 3.12, one would get the ground state density n_0.

3.2.2 Kohn-Sham equations

The ground-state electron density can be in principle determined by solving the Euler equation (3.12); however, the exact form of the functional F[n] is unknown. Kohn and Sham proposed a scheme to solve the multielectronic problem in which, starting from a model of non interacting electron system, they obtain a single particle Schrödinger equation whose solution gives the same electron density of the interacting electron system. It is first convenient to define a new functional $G[n(\mathbf{r})]$, obtained from $F[n(\mathbf{r})]$ by subtracting the term of the electron-electron electrostatic repulsion:

$$G[n(\mathbf{r})] = F[n(\mathbf{r})] - \frac{1}{2} \int d\mathbf{r} \int d\mathbf{r}' \frac{n(\mathbf{r}) n(\mathbf{r}')}{|\mathbf{r} - \mathbf{r}'|} \tag{3.13}$$

It is than useful to extract the kinetic energy functional T_s of the non-interacting system from G[n($\mathbf{r}$)], isolating all the exchange and correlation many-body contributions:

$$G[n(\mathbf{r})] = T_s[n(\mathbf{r})] + E_{xc}[n(\mathbf{r})] \tag{3.14}$$

In this way the Total Energy functional expressed in equation (3.8) becomes:

$$E[n(\mathbf{r})] = T_s[n(\mathbf{r})] + \frac{1}{2} \int d\mathbf{r} \int d\mathbf{r}' \frac{n(\mathbf{r}) n(\mathbf{r}')}{|\mathbf{r} - \mathbf{r}'|} + \int n(\mathbf{r}) v(\mathbf{r}) d\mathbf{r} + E_{xc}[n(\mathbf{r})] \tag{3.15}$$

The variation of the previous expression as a function of the electron density at constant number of electrons N leads to the following Euler equation:

$$\mu = \frac{\delta T_s[n]}{\delta n} + \int \frac{n(\mathbf{r}')}{|\mathbf{r} - \mathbf{r}'|} d\mathbf{r}' + v(\mathbf{r}) + \frac{\delta E_{xc}[n]}{\delta n} \tag{3.16}$$

which can also be written as:

$$\mu = v_{KS}(\mathbf{r}) + \frac{\delta T_s[n]}{\delta n} \tag{3.17}$$

where $v_{KS}(\mathbf{r})$ is the Kohn-Sham potential consisting of the external potential, the classical Coulomb and the exchange-correlation potentials. If we express for the model of the non interacting electron system the electron density as a function of the one electron orbitals ψ_i:

$$n(\mathbf{r}) = \sum_{i=1}^{occ} |\psi_i(\mathbf{r})|^2 \tag{3.18}$$

This procedure leads to the following single particle eigenvalue equation:

$$h_{KS}\psi_i = \left[-\frac{1}{2}\nabla^2 + v_{KS}(\mathbf{r})\right]\psi_i = \sum_{j_1}^{N} \epsilon_{ij}\psi_j \tag{3.19}$$

Making use of the fact that the operator h_{KS} is Hermitian, a unitary transformation of the orbitals leads to the Kohn-Sham equation:

$$\left[-\frac{1}{2}\nabla^2 + v_{KS}(\mathbf{r})\right]\psi_i = \epsilon_i\psi_i \tag{3.20}$$

Once solved this equation, it is possible to obtain the electron density of the interacting system as a sum over each single particle orbital. This is probably the most important equation of the Density Functional Theory. It states that the motion of the interacting electrons can be treated exactly as a system of independent (i.e. non-interacting) particles. The electrons can be considered as if they move in a common effective potential v_{KS}. All the interaction between the electrons can be merged exactly into a single potential v_{KS}.

Although DFT is an exact theory of the ground state, it is affected by the limit that the expression of the exchange and correlation potential appearing in the Kohn-Sham potential is not known explicitly. Different formulations of this functional have been proposed in the literature, based on different theoretical arguments.

3.2.3 LDA and GGA exchange-correlation approximations

The whole complexity of the electron-electron interaction is confined in the exchange-correlation term. Since DFT does not provide the analytical expressions of the functional $E_{xc}[n]$, the practical application of the theory requires the choice of approximated forms for $E_{xc}[n]$. Over the years many approximate expressions have appeared, the most simple and widely used of which is the local density approximation (LDA) [73, 74]. In

a homogeneous gas of interacting electrons the density is constant and the exchange-correlation energy per particle $\epsilon_{xc}(n)$ is a function (not a functional) of the density. The total exchange-correlation energy is obtained by multiplying $\epsilon_{xc}(n)$ by the total number of electrons present in the gas:

$$E_{xc}[n] = N\epsilon_{xc}(n) \tag{3.21}$$

Within the local density approximation, the non-homogeneous electron gas is treated in complete analogy: the total exchange-correlation energy is obtained by accumulating the contributions from every portion of the non-uniform gas as if it was locally uniform:

$$E_{xc}^{LDA} = \int n(\mathbf{r})\epsilon_{xc}^{hom}\left(n(\mathbf{r})\right) d\mathbf{r} \tag{3.22}$$

In calculating the integral 3.22 the function $\epsilon_{xc}^{hom}(n)$ is evaluated for the local density $n(\mathbf{r})$ of the inhomogeneous system under consideration: $\epsilon_{xc}^{hom}(n) = \epsilon_{x}^{hom}(n) + \epsilon_{c}^{hom}(n)$ is the exchange and correlation energy per electron in the homogeneous electron gas of density n. LDA is exact for an uniform system and is expected to be valid for systems with slowly varying electron density. For all the other cases the LDA approximation is indeed uncontrolled; its justification relies mainly upon its ability to reproduce the experimental ground-state properties of a large number of solids. LDA performs best for metals, while for semiconductors and insulators the band gap is underestimated by up to 50 % in some cases, but this problem is not only pertinent to LDA, but also to the formally not-justified interpretation of the Khon-Sham eigenvalues as excitation energies.

A number of methods have been developed to correct the deficiencies of the LDA. For a system of nonuniform density, E_{xc} is no longer adequately reproduced by Eq. 3.22. A simple modification appears to be the inclusion of gradient terms ∇n, which leads to the Generalized Gradient Approximation (GGA) [75],

$$E_{xc}^{GGA} = \int f(n, \nabla n) d\mathbf{r} \tag{3.23}$$

Various recipes for constructing $f(n, \nabla n)$ have been proposed. The PBE (Pendew, Burke and Ernzerhof) form [76] is probably the simplest GGA functional. The form for the correlation in this case is expressed as the local correlation plus an additive term both of which depend upon the density gradient. For the calculations performed within this thesis we have employed the PBE functional because it was reported that it correctly reproduces structural, mechanical and electronic properties of bulk ZnO, ZnO surfaces and nanostructure [77–80].

3.2.4 LDA+U method

Studies based on LDA and GGA have been previously used to investigate electronic and structural properties of ZnO, and Zn-3d electrons were treated as valence electrons [81–83]. Although they could give a very accurate lattice constant, the results strongly underestimated the band gap and gave the energy of Zn-3d states too close to the VBM due to overestimation of the hybridization between Zn-3d and O-2p states. Several approaches have been proposed to address band gap underestimation. For example, Vogel et al. [84] studied the electronic structure by the method of LDA plus Self-Interaction Correction (LDA + SIC). Their results were in good agreement with the experimental value for the band gap and the bandwidth, but the d states were still 1 eV lower than the experimental one. On the other hand, LDA + U corrections have been proved to be an effective improvement of LDA results, especially for 3d-transition metal oxides [85].

The main idea of LDA+U is to separate electrons into the subsystems: localized for which Coulomb interaction should be taken into account by a term $\frac{1}{2}U\sum_{i\neq j} n_i n_j$ (n_i are the orbital occupancies) and delocalized electrons which could be described by using an orbital independent one-electron potential (LDA). This LDA+U functional is expressed as,

$$E^{LDA+U}[n] = E^{LDA}[n] + E^{U}[n_i^\sigma] - E^{dc}[n_i^\sigma] \tag{3.24}$$

$E^{dc}[n_i^\sigma]$ is the double counting term. Because we add explicitly the Hubbard term, we have to remove the energy contribution of these orbitals included in the LDA functional in so as to ensure their contribution is not counted twice. $E^{dc}[n_i^\sigma]$ is approximated as mean-field value of the Hubbard term in the DFT. $\frac{1}{2}U\sum_{i\neq j} n_i n_j$ is the double counting term, and $UN(N-1)/2$, where $N = \sum_i n_i$.

Therefore:

$$E^{LDA+U}[n] = E^{LDA}[n] + \frac{U}{2}\sum_{i\neq j} n_i n_j - \frac{UN(N-1)}{2} \tag{3.25}$$

We can obtain the orbital eigenvalue by taking the derivative of the total energy with respect to the occupation number of that orbital. For LDA+U, we get:

$$\epsilon_i = \frac{\delta E^{LDA+U}}{\delta n_i} = \epsilon_i^{LDA} + U(\frac{1}{2} - n_i) \tag{3.26}$$

This last expression shows that is the state that is occupied, its energy is shifted -U/2 and if it is not occupied, its energy is raised by U/2. The LDA+U potential would be:

$$V^{LDA+U}(r) = V^{LDA} + U(\frac{1}{2} - n_i)P_i \tag{3.27}$$

The operator P_i is the projection operator on the localized orbital. From this formulation of the potential, we can see that if the state i is initially occupied by less than half, the Hubbard potential is positive and tend to repulse electrons. On the other hand, if the occupation is more than half filled, the potential is attractive and encourage electrons to localized on this particular site.

3.2.5 Hellmann-Feynman theorem

If we suppose to know the ground state eigenfunction ψ_R for a system in a fixed configuration of nuclei $\{R_\mathbf{A}\}$, solving the equation (3.4), the energy will be given by:

$$E = \frac{<\psi_R|H(\{R_\mathbf{A}\})|\psi_R>}{<\psi_R|\psi_R>} \tag{3.28}$$

Thus, the force on a nucleus n will be given by the negative gradient of the energy with respect to its coordinates (R_n):

$$\mathbf{F}_n = -\nabla_n E = -\nabla_n \left[\frac{<\psi_R|H(\{R_\mathbf{A}\})|\psi_R>}{<\psi_R|\psi_R>}\right] \tag{3.29}$$

When deriving the term at the right side of this equation, one must observe that not only the Hamiltonian but also the ground state depend on the particular configuration R. The Hellmann-Feynman theorem [86, 87] states that this dependence can be neglected if ψ_R is an eigenstate of the Hamiltonian. Thus, equation (3.29) gives:

$$\nabla_n E = \frac{<\psi_R|\nabla_n H(\{R_\mathbf{A}\})|\psi_R>}{<\psi_R|\psi_R>} \tag{3.30}$$

This means that in order to obtain the forces acting on the atoms in a particular geometric configuration, it is enough to know the explicit dependence of the Hamiltonian on the nuclear coordinate of the system. Once the forces acting on atoms are known one can integrate the classical equation of motion and study the evolution of the system, or simply minimize them in order to obtain equilibrium (or minimum energy) structures.

3.3 Wannier functions

The electronic ground state of a periodic system is usually described in terms of extended Bloch orbitals, simultaneous eigenstates of the periodic Hamiltonian and of the direct lattice translations. An alternative representation in terms of localized orbitals was proposed by Gregory Wannier in 1937 [88]; besides its theoretical relevance in several areas of solid-state theory, it has gained recent prominence due to its connection with the Berry-phase theory of bulk polarization. The connection between the Bloch

representation and the Wannier representation is realized by families of transformations in a continuous space of unitary matrices, and carries a large degree of arbitrariness. By transforming the occupied electronic manifold into a set of maximally-localized Wannier functions (MLWFs), it becomes possible to obtain an enhanced understanding of chemical coordination and bonding properties via analysis of factors, such as, changes in shape or symmetry of the MLWFs, or changes in the locations of their centers of charge. In particular, the charge center of a MLWF provides a kind of classical correspondence for the "location of an electron" (or electron pair) in a quantum-mechanical insulator. This analogy is extended further by the modern theory of bulk polarization [89, 90], which directly relates the vector sum of the centers of the Wannier functions to the macroscopic polarization of a crystalline insulator. Thus, the heuristic identification by which the displacements of the Wannier centers provide a microscopic map of the local polarization field is augmented, via the theory of polarization, by an exact statement relating the sum of displacements to the exact quantum-mechanical polarization of the system.

The one-particle effective Hamiltonian $\hat{H}$ that commutes with the lattice-translation operator $\hat{T}_R$, allowing one to choose as common eigenstates the Bloch orbitals $|\psi_{nk}\rangle$,

$$[\hat{H}, \hat{T}_R] \Rightarrow \psi_{ik}(r) = e^{i\phi_i(k)}\mu_{ik}(r)e^{ik.r}, \tag{3.31}$$

where $\mu_{nk}(r)$ has the periodicity of the Hamiltonian. There is an arbitrary phase $\phi_n(k)$, periodic in reciprocal space, that is not assigned by the Schrödinger equation and that we have written out explicitly. We obtain a (non-unique) Wannier representation using any unitary transformation of the form $\langle nk \mid Rn\rangle = e^{i\varphi_n(k)-ik.R}$:

$$\langle R_n| = \frac{V}{(2\pi)^3}\int_{BZ} \langle\psi_{nk}|\, e^{i\varphi_n - ik.R}dk. \tag{3.32}$$

Here V is the real-space primitive cell volume, and $\varphi_n(k+G) = \varphi_n(k)$, for any reciprocal-lattice translation G. It is easily shown that the $|R_n\rangle$ form an orthonormal set, and that two Wannier functions $|R_n\rangle$ and $|R'_n\rangle$ transform into each other with a translation of a lattice vector $R - R'$. The arbitrariness that is present in $\varphi_n(k)$ [or $\phi_n(k)$] propagates to the resulting Wannier functions, making the Wannier representation non-unique.

Thus, the most general operation that transforms the Bloch orbitals into Wannier functions is given by

$$\langle R_n| = \frac{V}{(2\pi)^3}\int_{BZ} \sum_{m=1}^{N} U_{mn}^{(k)}\, \langle\varphi_{mk}|\, e^{-ik.R}dk. \tag{3.33}$$

where $U_{mn}^{(k)}$ is a unitary matrix of dimension N which is the occupied states. Alternatively, we can regard this as a two-step process in which one first constructs Bloch-like orbitals

$$|\tilde{\varphi}_{nk}\rangle = \sum_{m=1}^{N} U_{mn}^{(k)} |\varphi_{mk}\rangle \tag{3.34}$$

and then constructs Wannier function $|w_n\rangle$ from the manifold of states $|\tilde{\varphi}_{nk}\rangle$. The extra unitary mixing may be optional in the case of a set of discrete bands that do not touch anywhere in the Brillouin zone, but it is mandatory when describing a case like that of the four occupied bands of silicon, where there are degeneracies at symmetry points in the Brillouin zone. An attempt to construct a single Wannier function from the single lowest-energy or highest-energy band would be doomed in this case, because of non-analyticity of the Bloch functions in the neighborhood of the degeneracy points. Instead, the introduction of the unitary matrices $U_{mn}^{(k)}$ allows for the construction of states $|\tilde{\varphi}_{nk}\rangle$ that are everywhere smooth functions of $\mathbf{k}$. In this case, the Wannier functions $w_n(r-R) = \langle R_n|$, can be shown to be well localized: for a $\mathbf{R}_i$ far away from $\mathbf{R}$, $w_n(r-R)$ is a combination of terms like $\int\limits_{BZ} u_{mk}(0)e^{ik.(R_i-R)}d\mathbf{k}$, which are small due to the rapidly varying character of the exponential factor.

3.3.1 Maximally-Localized Wannier Functions (MLWFs)

Several heuristic approaches have been developed that construct reasonable sets of Wannier functions, reducing the arbitrariness in the $U_{mn}^{(k)}$ with symmetry considerations and analyticity requirements [91], or explicitly employing projection techniques on the occupied subspace spanned by the Bloch orbitals [92]. At variance with those approaches, we introduce a well-defined localization criterion, choosing the functional

$$\Omega = \sum_n [\langle 0n| r^2 |0n\rangle - \langle 0n| r^2 |0n\rangle^2] = \sum_n [\langle r^2\rangle_n - \bar{r}_n^2] \tag{3.35}$$

as the measure of the spread of the Wannier functions. The sum runs over the n functions $|0n\rangle$; $\langle r^2\rangle_n$ and $\bar{r}_n = \langle r\rangle_n$ are the expectation values $\langle 0n| r^2 |0n\rangle$ and $\langle 0n| r^2 |0n\rangle$. Given a set of Bloch orbitals $|\varphi_{mk}\rangle$, the goal is to find the choice of $U_{mn}^{(k)}$ in Eq. 3.33 that minimizes the values of the localization functional (Eq. 3.35). We are able to express the gradient $G = \frac{d\Omega}{dW}$ of the localization functional with respect to an infinitesimal

unitary rotation of our set of Bloch orbitals

$$|u_{nk}\rangle \rightarrow |u_{nk}\rangle + \sum_m dW^{(k)}_{mn} |u_{mk}\rangle \,, \tag{3.36}$$

where dW an infinitesimal anti-unitary matrix $dW^\dagger = -dW$ such that

$$U^{(k)}_{mn} = \delta mn + dW^{(k)}_{mn} \tag{3.37}$$

This provides an "equation of motion" for the evolution of the $U^{(k)}_{mn}$, and of the $|R_n\rangle$ derived in Eq. 3.33, towards the minimum of Ω; e.g., in the steepest descent approach small finite steps in the direction opposite to the gradient decrease the value of Ω, until a minimum is reached.

3.3.1.1 Real-space representation

There are several interesting consequences stemming from the choice of Eq. 3.35 as the localization functional, that we briefly summarize here. Adding and subtracting the off-diagonal components $\tilde{\Omega} = \sum_n \sum_{Rm \neq 0n} |\langle Rm|r|0n\rangle|^2$, we obtain the decomposition,

$$\Omega = \Omega_1 + \tilde{\Omega} = \Omega_1 + \Omega_D + \Omega_{0D} \tag{3.38}$$

where Ω_1, $\tilde{\Omega}$, Ω_D, and Ω_{0D} are respectively

$$\Omega_1 = \sum_n \left[\langle 0n|r^2|on\rangle - \sum_{Rm} |\langle Rm|r|0n\rangle|^2 \right], \tag{3.39}$$

$$\tilde{\Omega} = \sum_n \sum_{Rm \neq 0n} |\langle Rm|r|0n\rangle|^2,$$

$$\Omega_D = \sum_n \sum_{Rm \neq 0n} |\langle Rm|r|0n\rangle|^2,$$

$$\Omega_{0D} = \sum_{m \neq n} \sum_R |\langle Rm|r|0n\rangle|^2.$$

It can be shown that each of these quantities is positive-definite (in particular Ω_1, see Ref. [93]); moreover, Ω_1 is also gauge-invariant, i.e., it is invariant under any arbitrary

unitary transformation Eq. 3.35 of the Bloch orbitals. The minimization procedure thus corresponds to the minimization of $\tilde{\Omega} = \Omega_D + \Omega_{0D}$. At the minimum, the elements $|\langle Rm|r|0n\rangle|^2$ are as small as possible, thus realizing the best compromise in the simultaneous diagonalization, within the space of the Bloch bands considered, of the three position operators x, y and z.

3.3.1.2 Reciprocal-space representation

As shown by Blount [94], matrix elements of the position operator between Wannier functions take the form

$$\langle Rn|r|0m\rangle = i\frac{V}{(2\pi)^3}\int dk e^{ik.R}\langle u_{nk}|\nabla_k|u_{mk}\rangle \tag{3.40}$$

and

$$\langle Rn|r^2|0m\rangle = -\frac{V}{(2\pi)^3}\int dk e^{ik.R}\langle u_{nk}|\nabla_k^2|u_{mk}\rangle. \tag{3.41}$$

These expressions provide the needed connection with our underlying Bloch formalism, since they allow us to express the localization functional Ω in terms of the matrix elements of ∇_k and ∇_k^2. In addition, they allow us to calculate the effects on the localization of any unitary transformation of the $|u_{nk}\rangle$ without having to perform expensive recalculation (at least when plane-wave basis sets are used) of scalar products. We thus determine the Bloch orbitals $|u_{mk}\rangle$ on a regular mesh of k-points, and finite differences is used to evaluate the above derivatives.

3.4 Practical aspects of DFT implementation

In the following paragraphs some practical aspects regarding DFT implementation will be discussed, namely, the use of pseudopotential, the use of a plane wave basis set to expand the system wave-function and the concept of supercell to deal with non-periodic structures.

3.4.1 Plane Wave basis set

Ions in a perfect crystal are arranged in a regular periodic way (at $0K$), therefore the external potential felt by the electrons is periodic and the period is the same as the

length of the unit cell (l). The external potential on an electron at $\mathbf{r}_i$ can be expressed as $V(\mathbf{r}) = V(\mathbf{r} + l)$. For these kind of systems, the Bloch Theorem holds, and the wavefunction can be written as the product of a cell periodic part and a wave-like part:

$$\phi_{i,\mathbf{k}} = u_{i,\mathbf{k}}(\mathbf{r})e^{i\mathbf{k}\cdot\mathbf{r}} \tag{3.42}$$

where $u_{i,\mathbf{k}}(\mathbf{r})$ is a function that has the lattice periodicity. The periodic part of the wave function can be expanded using a basis set of plane waves whose wave vectors $\mathbf{G}$ are the reciprocal lattice vectors of the crystal:

$$u_{i,\mathbf{k}}(\mathbf{r}) = \sum_{\mathbf{G}} c_{i,\mathbf{G}} e^{i\mathbf{G}\cdot\mathbf{r}} \tag{3.43}$$

therefore each electronic wave function can be written as a linear combination of plane waves (PW):

$$\phi_{i,\mathbf{k}} = \sum_{\mathbf{G}} c_{i,\mathbf{k}+\mathbf{G}} e^{i(\mathbf{k}+\mathbf{G})\cdot\mathbf{r}} \tag{3.44}$$

the $c_{i,\mathbf{k}+\mathbf{G}}$ are unknown and must be determined for each specific case. The plane-waves basis set is in principle infinite, but in real calculations it is reduced to a finite one by truncating the sum over $\mathbf{G}$ to include only those plane waves with a kinetic energy $E_k = \frac{1}{2}(\mathbf{k} + \mathbf{G})^2$ less than a given energy cutoff (E_{cut}). This truncation will lead to an error in the computed total energy. At variance with other techniques (and basis sets) the convergence of the plane-wave basis set (and thus the error) can be controlled simply by increasing the cutoff energy. When pseudopotentials are used (see next paragraph) to include the electron/ion interaction, it is possible to reduce sensibly the cutoff energies, without loosing accuracy.

3.4.2 The Pseudopotential approximation

A further approximation for the calculation of the electronic properties of a system consists in the use of pseudopotentials (PP). In most molecular or solid state systems, it is possible to separate atomic states into valence states, which determine the bonding properties, and core states which are much deeper in energy and can therefore be considered as chemically inert. In the pseudopotential scheme the electronic problem is simplified by including only the valence states. The core states, which can be considered as essentially unchanged with respect to the free atom, affect the valence wave functions only because of the orthogonality conditions. These inert states can be eliminated by replacing the true atomic Coulomb potential by a pseudopotential, designed in such a way that the effect of the core states on the valence states is properly reproduced. Since the number of core states per species is not fixed, this does not impose limitations on

the accuracy of the method.
A possible way of constructing pseudopotentials, within the framework of DFT, has been proposed by Hamann, Schlüter and Chiang [95]. For most of the elements, a fully local pseudopotential cannot reproduce accurately the properties of the all-electron wave function, thus a non-local form is proposed in which a different pseudopotential, v_l, is used for each angular momentum channel l:

$$v_{ps}(\mathbf{r}) = \sum_{l=0}^{\infty} v_l(r)\hat{P}_l \tag{3.45}$$

Here $\hat{P}_l$ is a projector onto the l-th angular momentum. Since for high l (e.g $l \geq 2$ for most elements) the l component of the wavefunction is very small in the core region, v_l can eventually be taken to be independent of l. The pseudopotentials are derived in the case of the free atom and required to satisfy the following conditions:

- for every angular momentum, the pseudo-eigenstates are required to be equal to the all-electron eigenstates;
- a core radius cutoff (r_c) is defined beyond which the pseudo-wavefunction matches the all-electron wave-function;
- in the core region, the pseudo-wavefunction is nodeless and carries the same charge as the all electron wavefunction (norm conserving condition).

See Fig. 3.1 for a schematic illustration of this construction.
Pseudopotentials are usually required to be applicable to a number of different configurations (solid, molecule, ionized atom...) for the atomic species: this constrain is known as transferability.

The replacement of the true ionic potential by a weaker pseudopotential allows the electronic wavefunction to be expanded using fewer plane-waves than would be needed to expand the wavefunction in a full ionic potential. The rapid oscillations of the valence wavefunctions in the cores of the atoms are removed, and the core electron states are no longer present.

The pseudopotential approximation has a number of other advantages in addition to reducing the number of plane-waves required to expand the electronic wavefunctions. The removal of the core electrons means in fact that less electronic states have to be calculated. Most importantly, the total energy of the valence electron system is typically a thousand times smaller than the energy of the all-electron system. The difference between the electronic energies of different ionic configurations appears almost totally in

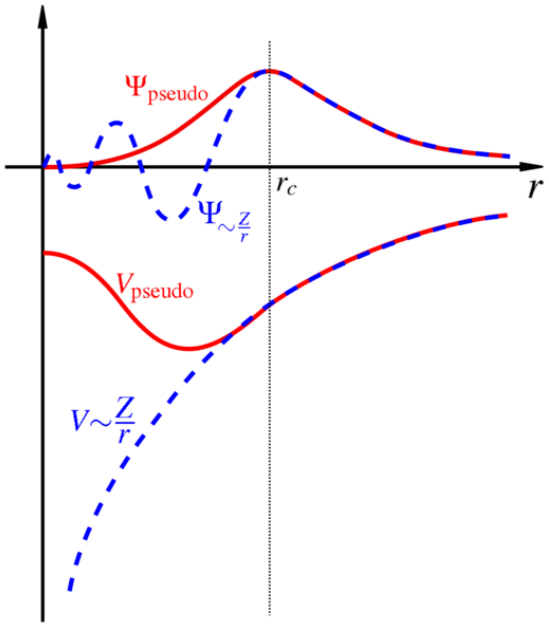

FIGURE 3.1: Schematic illustration of all electron (solid lines) and pseudoelectron (dashed lines) potential and their corresponding wave functions. The radius at which all-electron and pseudo-electron values match is designed as r_c.

the energy of the valence electrons, so that the accuracy required to determine energy differences between ionic configurations in a pseudopotential calculation is much smaller than the accuracy required in the all electron calculation. Of course, the total energy is meaningless, in the pseudopotential approach, and only differences count. This automatically improves the overall accuracy of the method, since smaller values become meaningful. Convergence tests are needed in order to be sure to have chosen a cutoff able to reproduce structural experimental data and converged energy differences.

3.4.2.1 Ultrasoft pseudopotentials

Ultrasoft pseudopotentials (USP) were proposed by Vanderbilt and coworkers [96] where norm-conserving condition were relaxed so that a much softer potentials were generated. In this scheme the pseudo-wave-functions are allowed to be as soft as possible within the core region, so that the cutoff energy can be reduced dramatically. Technically, this is achieved by introducing a generalized orthonormality condition. The electron density given by the squared moduli of the wave functions has to be augmented in the core region in order to recover the full electronic charge. The electron density is thus subdivided into a smooth part that extends throughout the unit cell and a hard part localized in the core regions.

USP generation algorithm guarantees good scattering properties over a pre-specified

energy range, which results in much better transferability and accuracy of pseudopotentials. USP usually also treats "shallow" core states as valence by including multiple sets of occupied states in each angular momentum channel. This also adds to high accuracy and transferability of the potentials, which made them attractive choice in this study. For more details see Refs. [97, 98].

3.4.3 Reciprocal-space integration and k points sampling

When considering periodic systems, in the Kohn-Sham calculation scheme the valence electron density and the band structure energy are defined as sum over the entire BZ as follows:

$$n(\mathbf{r}) = \sum_{i=0}^{occ} \sum_{\mathbf{k}\in BZ} |\phi_{v,\mathbf{k}}(\mathbf{r})|^2 \tag{3.46}$$

$$E_{band} = \sum_{i=0}^{occ} \sum_{\mathbf{k}\in BZ} \epsilon_{v,\mathbf{k}} \tag{3.47}$$

for an infinitely periodic system the discrete sums are replaced by integrals over the Brilluoin Zone (BZ) and an average over the BZ of the **k**-dependent functions is actually performed. In practice, it is possible to approximate the integral over the BZ by using a selected set of **k**-points, exploiting both the space group of the crystal, and a clever sampling of the BZ. Due to the group symmetry the sum over **k** can be restricted to the irreducible part of the BZ (IBZ), and then sample this zone with a special point technique. Typically, one employes a Monkhorst-Pack grid [99], which consists of a mesh of equally spaced points along the three reciprocal space primitive vectors and it is defined by three integer (n_x n_y n_z). These n_i represent the number of sampling point along each lattice vectors, and of course, the larger are n_i the finer the grid will be and the more accurate will be the calculated electronic density. The actual n_i values to be used generally depend on the problem that needs to be solved; usually convergence test, at increasing n_i, have to be performed to determine for each specific system the grid that gives accurate results. For example, systems with a gap in the energy spectrum typically require fewer points, whereas in case of metallic systems a much denser **k**-mesh must be employed, ensuring good sampling of the Fermi surface.

3.4.4 Supercells for Nanowires and Surfaces

The supercell approach allows to deal with aperiodic configurations of atoms within the framework of Bloch theorem, allowing to use a PW basis set. In this approach, when dealing, for example with surfaces, that may have periodicity in the plane of the

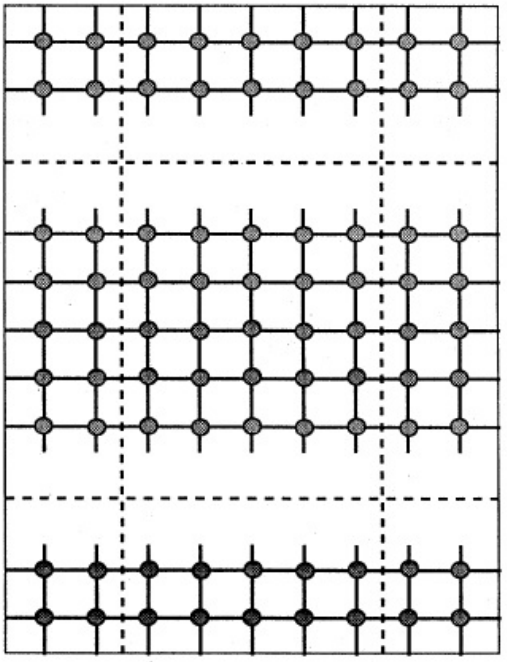

FIGURE 3.2: Schematic illustration of a supercell geometry for a surface of a bulk solid, taken from [5]. The supercell is the area enclosed by the dashed lines: it contains a crystal slab and the vacuum region.

surface, but without periodicity in the perpendicular direction, one simply constructs a large unit cell containing the configuration of interest included in a vacuum region; some precautions must be taken, depending on the system. To ensure that the results of the calculation accurately represent an isolated surface, the vacuum region must be wide enough so that faces of adjacent crystal slabs (replicas) do not interact across the vacuum region; the slab itself must be thick enough so that the two surfaces do not interact through the bulk crystal, and furthermore bulk properties themselves are accurately reproduced. The supercell for a surface calculation is illustrated schematically in Fig. 3.2. Similarly, nanostructures such as nanowires can be studied in this approach, but the supercell must be large enough so that the interaction between the object and its images in the neighboring cells are negligible. Also when using only the Γ point in the reciprocal space integration, it is necessary to use supercells, i.e. cells which are not primitive and contain more than one unit cell. Replicating a cell in the direct space is in fact equivalent to fold the Brillouin Zone (BZ) in the reciprocal space. When doing so, the Γ point of the supercell will map a certain number of $\mathbf{k}$ points of the irreducible BZ. If the cell is big enough, the number of $\mathbf{k}$ points mapped by Γ is sufficient to get a wavefunction which can accurately reproduce the properties of the studied material. Nevertheless since the computational cost of the simulation increases as the supercell dimensions increase, a compromise must be reached.

3.4.5 Climbing Image Nudged Elastic Bands (CI-NEB)

An important problem in theoretical chemistry and condensed matter physics is the calculation of transition rates, for example, rates of chemical reactions or diffusion events. Harmonic approximation to transition state theory (hTST) [100] is routinely used to study diffusion and reactions in crystals or crystalline surfaces.

A path that connects the initial and final states is chosen such that it has the greatest statistical weight and is considered as the minimum energy path (MEP) [101]. At any point along the path, the force acting on the atoms is only pointing along the path, and is stationary for any perpendicular degree of freedom. The maxima on the MEP are saddle points on the potential energy surface. The relative distance along the MEP is a natural choice for a reaction coordinate, and at the saddle point the direction of the reaction coordinate is given by the normal mode eigenvector corresponding to negative curvature.

The MEP is found by constructing a set of images (replicas) of the system, typically on the order of 4–20, between the initial and final state. A spring interaction between adjacent images is added to ensure continuity of the path, thus mimicking an elastic band. An optimization of the band, involving the minimization of the force acting on the images, brings the band to the MEP.

The nudged elastic band (NEB) method is an efficient method to find the MEP between a given initial and final state of a transition. An elastic band with N+1 images can be denoted by $R_0, R_1, R_2, ..., R_N$, where the endpoints, R_0 and R_N,are fixed and given by the energy minima corresponding to the initial and final states. The N-1 intermediate images are adjusted by the optimization algorithm. The total force acting on an image is the sum of the spring force along the local tangent and the true force perpendicular to the local tangent

$$F_i = F_i^S\Big|_{\parallel} - \nabla E(R_i)\Big|_{\perp}, \tag{3.48}$$

where the true force is given by

$$\nabla E(R_i)\big|_{\perp} = \nabla E(R_i) - \nabla E(R_i).\hat{\tau}_i. \tag{3.49}$$

Here, E is the energy of the system, and is a function of all the atomic coordinates, and $\hat{\tau}_i$ is the normalized local tangent at image i. The spring force is

$$F_i^S\big|_{\parallel} = k(\big|R_{i+1} - R_i\big| - \big|R_i - R_{i-1}\big|)\hat{\tau}_i \tag{3.50}$$

where k is the spring constant. An optimization algorithm is then used to move the images according to the force in Eq. 3.48: a projected velocity Verlet algorithm in the code used in this work. The images converge on the MEP with equal spacing if the spring constant is the same for all the springs. Typically none of the images lands at or even near the saddle point and the saddle point energy needs to be estimated by interpolation.

The climbing image NEB (CI-NEB) method constitutes a small modification to the NEB method. Information about the shape of the MEP is retained, but a rigorous convergence to a saddle point is also obtained. This additional feature does not add any significant computational effort. After a few iterations with the regular NEB, the image with the highest energy i_{max} is identified. The force on this one image is not given by Eq. 3.48 but rather by

$$F_{i_{max}} = -\nabla E(R_{i_{max}}) + 2\nabla E(R_{i_{max}})\big|_{\|}$$

$$-\nabla E(R_{i_{max}}) + 2\nabla E(R_{i_{max}}).\hat{\tau}_{i_{max}}\hat{\tau}_{i_{max}} \tag{3.51}$$

This is the full force due to the potential with the component along the elastic band inverted. The maximum energy image is not affected by the spring forces. Qualitatively, the climbing image moves up the potential energy surface along the elastic band and down the potential surface perpendicular to the band. The other images in the band serve the purpose of defining the one degree of freedom for which a maximization of the energy is carried out. Since the images in the band eventually converge to the MEP, they give a good approximation to the reaction coordinate around the saddle point [102].

Chapter 4

ZnO test calculations

In this chapter we briefly discuss the results for bulk ZnO, which is the reference structure for all the calculations presented in the next chapters. Physical properties of ZnO are determined and compared to those in literature to test our computational approach and parameters. Furthermore, the role of hydrogen as source of n-type conductivity in ZnO is studied.

4.1 Introduction

ZnO is a polar semiconductor, whose wide band gap and large excitonic energy have inspired several applications in electronics and optoelectronics [8, 80]. Physical properties of ZnO have been extensively studied both experimentally and theoretically (see Refs. [8, 29, 30, 103–105]), thus the purpose of this section is to test the reliability of our computational parameters in describing ZnO.

One of the most serious challenges to the development of ZnO-based technologies for electronics is controlling its electrical properties. As-grown ZnO shows high levels of unintentional n-type doping, with carrier concentrations typically varying from $\sim 10^{16}$ to $\sim 10^{17}$ electrons cm^{-3} [27]. This n-type conductivity has often been attributed to intrinsic defects, particularly Zn interstitials and O vacancies, but the subject is still controversial [27, 106, 107]. In this chapter, hydrogen contamination is investigated as possible source of n-type conductivity of ZnO.

4.2 Computational details

The DFT calculations presented in this thesis have been performed with the Quantum Espresso suite [108]. In these calculations, we have used ultrasoft pseudopotential plane wave implementation of DFT, with energy cutoff of 28 Ry (280 Ry) for the wavefunctions (charge density). The exchange-correlation energies were calculated by using the Perdew-Burke-Ernzerhof [109] approximation of the generalized gradient approach. Converged (8×8×8) Monkhorst-Pack grids [110] have been employed for the k-point sampling and all atomic positions have been relaxed with the conjugated gradient algorithm till all forces become smaller than 0.01 eV/Å. In the case of nanowires and surfaces, the computational details are presented in Appendix A.

4.3 Structural and mechanical properties

Using the computational parameters presented in previous section, structural and mechanical properties of bulk ZnO are determined to test reliability of our approach. These test are performed for the wurtzite structure, which is the stable structure of ZnO at ambient condition. The lattice parameters determined by various experimental measurements and theoretical calculations (see Ref. [8]) are in good agreement with our results. Concerning its mechanical properties, ZnO is a relatively soft material; with an average

Paramters	current works (GGA)	Others (GGA,LDA Ref. [104])	Expt (Ref. [104])
a($\AA$)	3.289	3.282, 3.192	3.25
c($\AA$)	5.315	5.291, 5.163	5.207
E_g(eV)	0.70	0.74, 0.78	3.34
B_0 (GPa)	126	128, 161	142
B'$_0$ (GPa)	4.88	5.75 (Ref. [8])	3.6
e_{31}(C/m^2)	-0.44	-0.51	-0.51, -0.62
e_{33}(C/m^2)	1.09	0.89, 1.21	0.96, 1.22
P_Z (C/m^2)	-0.036	-0.057, -0.050	-0.07
$\varepsilon^{eff}{}_{33}$(C/m^2)	1.29	1.28 (Ref. [111])	1.22 (Ref. [17])

TABLE 4.1: Structural and Mechanical Properties of ZnO calculated with DFT method and their comparison with previous theoretical and experiments works. B_0 and B'$_0$ are the bulk modulus and bulk hardness, respectively. e_{31}, e_{33} represent piezoelectric constants, while P_Z and $\varepsilon^{eff}{}_{33}$ are the spontaneous polarization and effective piezoelectric constant, respectively.

bulk hardness of ∼5 GPa for c-axis oriented crystals compared to 12 and 15 GPa for Si and GaN respectively [112]. Furthermore, the piezoelectric constants (e_{31}, e_{33}, and $\varepsilon^{eff}{}_{33}$) compares well with those obtained by other groups; this gives us confidence to apply the approach to nanostructure as will be shown in the next chapter 5.

4.4 Role of hydrogen interstitial in n-type conductivity

The source of intrinsic n-type conductivity of as-grown ZnO has for long been attributed to oxygen vacancies [106, 107]; however this claim has been questioned by recent studies that have suggested hydrogen as the most probable source [113–115]. Detection of hydrogen atoms adsorbed on surface and subsurface region of ZnO with standard surface characterization techniques, such as, low energy electron diffraction (LEED), transmission electron microscopy (TEM), and X-photoelectron spectroscopy (XPS) is difficult, thus dedicated experimental measurements are required, such as low/medium energy ion scattering (L/MEIS). With this respect, theoretical results are highly desirable and needed to complement experimental investigations and may help in understanding adsorbate geometry.

In this section, we focus on understanding structural and electronic properties of interstitial hydrogen in ZnO. This is motivated by carefully performed experiments that have demonstrated reversible loading and depletion of interstitial hydrogen on a perfect ZnO crystal, and how this has direct effect on the electrical properties of the crystal [114].

4.4.1 Structural properties

Experimental studies have revealed that interstitial hydrogen in ZnO is located at bond-centered (BC) position between O and Zn atoms [116, 117], whereas other experimental studies have suggested anti-bonding (AB) site as being the preferred site [118]. Our *ab initio* calculations showed that the BC site of interstitial hydrogen is energetically preferred, consistently with previous theoretical studies [119, 120]. Our results show

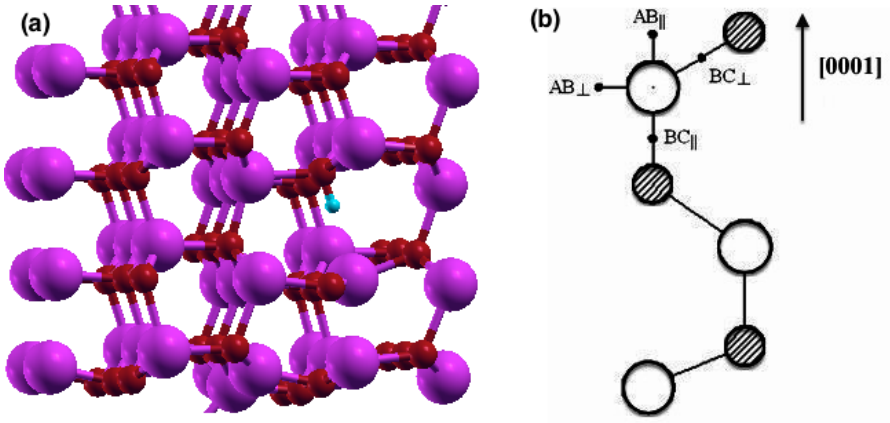

FIGURE 4.1: (a) Ball and stick model of the relaxed atomic positions of surface with interstitial hydrogen. Red, pink, and blue spheres represent zinc, oxygen, and hydrogen atoms, respectively. (b) Various interstitial sites for hydrogen. BC and AB denote the bond-center and anti-bonding site, respectively. Symbols ∥ and ⊥ shows the configuration of O–H bond parallel and perpendicular to c-axis, respectively.

that when hydrogen with neutral charge is introduced in ZnO as an interstitial with a concentration of 0.70 % a stable configuration is obtained with the formation of a strong O–H bond on BC‖ site, and breaking Zn–O bond, as shown in Fig. 4.1. Large lattice relaxations occur around the hydrogen interstitial; in particular, the Zn is displaced by a distance equal to 50% of the bond length (1.0 Å), to a position slightly beyond the plane of its nearest neighbors, while the O atom moves outward by 11% of the bond length, as shown in Fig. 4.1(**a**).

Previous studies have shown that both substitutional and interstitial forms of hydrogen have low formation energies in ZnO [27], and for this reason it can be easily incorporated either intentionally or unintentionally in significant concentration. Interstitial hydrogen is highly mobile and can be removed by annealing at relatively modest temperatures ($\sim$ 420 K); however, hydrogen also exist as thermally stable donor that persist even upon annealing at temperatures up to high temperature $\sim$ 800 K eventually as substitutional hydrogen [121].

4.4.2 Electronic properties

The density of states of pure and hydrogen doped ZnO are presented in Fig. 4.2 calculated at GGA + U level [122].

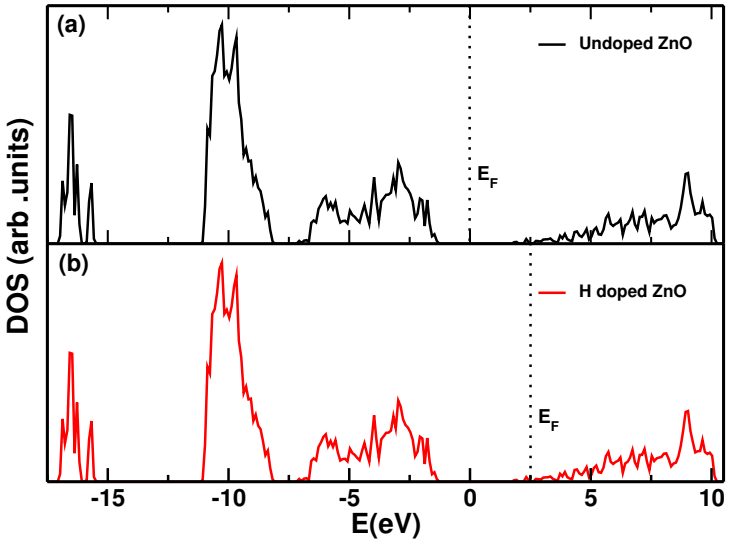

FIGURE 4.2: Density of state plots for (**a**) undoped and (**b**) hydrogen doped ZnO surface. Dotted line show the location of Fermi level and VBM is set to zero energy.

While the unroped system is semiconducting as demonstrated by location of Fermi level (E_F) in the band-gap, introduction of hydrogen shifts E_F to the CB, hence the system becomes conductive. This is attributed to the fact that hydrogen acts as a shallow donor populating the CB with electrons. We will thus consider in the following chapters H as

responsible of n-type conductivity, as observed in most common as-grown ZnO experimental structures [113–115, 118].

It should be pointed out that hydrogen is by no means the only source of n-type conductivity of ZnO. Recent studies have identified Al, Ga, and Si as present in as-grown ZnO and act as shallow donor [123], but do not occur in high concentration to explain the unintentional n-type conductivity of ZnO crystals.

Chapter 5

Piezoelectric properties of ZnO NWs

As introduced in Chapter 1, an innovative approach for converting mechanical energy into electricity has been recently proposed by Wang and coworkers [14] which relies on the use of piezoelectric ZnO NWs. ZnO has several key advantages in these area, since, beside being a piezoelectric semiconductor, it is biologically safe and it occurs in a wide range of 1D and 2D nanostructures which can be integrated with flexible organic substrates for future flexible, stretchable, and portable electronics. Although these applications are promising, they are still away from being commercially available, mostly due to issues of reliability and robustness [124], as well as performance optimization, which remains to be addressed. For example, it is desirable to know which set of nanowire morphological (diameter, length), structural (crystal structure, defect type and density, etc.), and electrical properties (conductivity, polarizability) gives the best performance. Some experimental investigation have proven an enhancement of the mechanical [16], and electromechanical [125] properties of nanowires with diameter below 100 nm and, as such, they evidenced that piezoelectric harvesting is more effective with nanostructures rather than with thin films or bulk ZnO. On the contrary, other experimental investigations did not find relevant differences in the piezoelectric behavior of bulk and nanostructured material. With this respect, development of detailed theoretical approaches is desirable to complement and support experimental work and unambiguously characterize the physical properties of nanosized materials. Indeed, the challenging nature of experimentation at the nanoscale requires comparison between measurements and theoretical studies such as first principle calculations in order to discard methodological artifact. In this chapter, we investigate the piezoelectric and

mechanical response of ZnO nanowires in terms effective piezoelectric constant and effective strain energy. These quantities are compared with the ones reported in literature and are connected to the to energy harvesting capability of ZnO nanowires.

5.1 State of the art

Since the successful demonstration of energy scavenging capabilities of ZnO NWs [14], numerous studies have been performed to characterize their electro-mechanical behavior. Using piezoelectric force microscopy (PFM) on individual ZnO NWs grown along the [0001] axis, piezoelectric constant was measured to be 14.3 to 26.7 pm/V [3], higher than the bulk value ($\sim$ 9.9 pm/V). A similar study for ZnO NWs with diameter in the range of 150–500 nm, and length of 400–600 nm, reported a variation of piezoelectric constant from 0.4–9.5 pm/V [126]. However, other studies have questioned the validity of these results [127], therefore for practical application of ZnO, better understanding of its structural and electric properties are still needed. Beyond this, a better knowledge of the elastic response of nanostructures to external deformations would be beneficial to prevent failure and fractures of novel nanodevices. Furthermore, controversial results appear in the literature, depending on the material, on the nanostructure form, and on the growth direction [15, 127, 128]. From the experimental point of view, indeed, the characterization of mechanical properties of NWs can be severely affected by artifacts linked to the specific experimental set-up, such as AFM on a single sample or a network, measurements performed on clamped or free standing samples, on conductive versus insulating substrates, etc. (see e.g. H. D. Espinosa *et al.*[15]).
On the theoretical front, as well, while it has been assessed that spontaneous polarization of wires strongly depends on the nanostructure size [78], the question whether size affects piezoelectric properties still remains open. In particular, Cicero and co-workers [78] established the existence of a minimum diameter below which the NW polarization field is inverted with respect to bulk because of large surface effects in small nanostructures. As for the piezoelectric response of ZnO NWs, Xiang *et al.*[18] proposed that NWs with diameter larger than 2.8 nm tend to have almost constant effective piezoelectric constants (close to the bulk value), while for smaller NWs, they found a non-trivial dependence of the electromechanical coupling on the radius as a result of two competitive effects, i.e., increase of the lattice constant along with decrease of the NW radius. On the contrary a giant piezoelectric response was predicted by Agrawal *et al.*[19] of approximately 2 orders of magnitude larger than bulk for NWs with diameter lower than 1 nm; such increase would be attenuated for NWs with diameters exceeding 1.5 nm. It is noteworthy that effective piezoelectric coefficients of ZnO NWs reported in the above mentioned studies [18, 19, 129] were all calculated using Berry-phase method within the

modern theory of polarization [47, 89], yet leading to dramatically different results, as shown in Table 5.1.

e_{33}^{eff} (Cm^{-2})	NW1	NW2	NW3	NW4	NW5	Bulk
Ref. [19]		50.2	18.1	14.1		1.18
Ref. [18]	4.77	2.21	1.82	1.74	1.62	1.29
Ref. [129]	6.35	2.59	1.87	1.84		
Ref. [111] Expt						1.22

TABLE 5.1: Effective piezoelectric constant e_{33}^{eff} of ZnO NWs of varying diameter compared to bulk value.

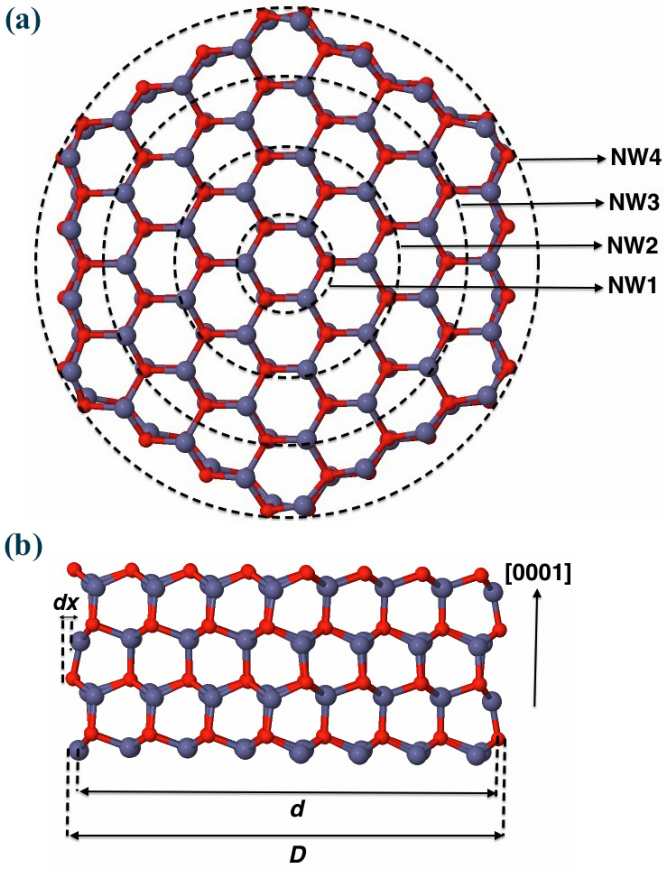

FIGURE 5.1: (**a**) Cross section view of ZnO NWs with different radii as indicated by dashed circles and labelled NW1, NW2, NW3, and NW4. (**b**) Side view of the largest wire, NW4, (two repetition of the unit cell are shown along the [0001] wire axis). Grey (red) spheres represent Zinc (Oxygen) atoms; d and D represent two possible choices of the NWs diameter, calculated either when atoms are considered as point charges or as spheres, respectively; dx indicates the uncertainty induced by surface relaxation.

The origin of the above mentioned debate is most probably due to the sources of uncertainty, that, although often neglected, severely alter the volume definition of a nanostructure: these are namely surface relaxation (dx) and ionic radius (see Fig. 5.1). While

the first source of error can be easily accounted for via accurate calculations or dedicated experimental techniques, the second issue is more tricky. The volume definition used to calculate polarization of nanowires is usually not mentioned in previously published papers; however, the nanowire size can be defined through its diameter either by considering the atoms as point charges or as finite spheres (e.g. via the ionic radius): this is enough to obtain an uncertainty of few Angstroms on its value ($\simeq$ 2Å in the case of ZnO). This uncertainty on the diameter has increasing relevance at the nanometer scale, and indeed leads to a large uncertainty in the volume occupied by the nanostructure (up to 70 % in the case of the smallest NW considered in this work): the smaller the structures the larger is the uncertainty. As such, all the physical quantities normalized to volume, like spontaneous polarization and piezoelectric constants, present large variability depending on the particular volume definition employed in the calculations.

5.2 Definition of Local dipole and effective piezoelectric constant

In this work, we propose a rigorous method to overcome the problem associated with volume definition of a nanostructure: we adopt a scheme that passes through a normalization in terms of number of formula units per supercell without loss of generality. This approach was successfully employed by Cicero and coworkers [78] to describe the size effect on the spontaneous polarization of nanowires, while correctly reproducing bulk values at increasing diameter. In particular, we take advantage of the Wannier Functions (WFs) definition that allows one to calculate local contributions (one for each ZnO couple) to the average dipole of a system. The procedure allows to define in a unique rigorous way the different contributions (bulk vs. surface) relevant to evaluate the nanostructure response to external deformation (thus assigning correct to NWs due to size), thus finally opens the possibility for an optimized design of novel piezo-devices at the nanoscale.

According to the modern theory polarization [47, 90], the macroscopic polarization of a periodic structure, P, is defined only with respect to a reference system; for example, in the case of wurtzite (WZ) one can choose the zincblende (ZB) phase, since the two structures are equivalent up to third neighbors [1]. In terms of WFs [93] polarization can be written as

$$P = P_{WZ} - P_{ZB} = \frac{e}{V}\sum_I Z_I \Delta R_I - \frac{2e}{V}\sum_i \Delta r_i^W \tag{5.1}$$

[1] In experiment, only polarization changes are accessible; similarly the polar behavior of a system is defined and calculated as difference with respect to a reference structure: one usually takes a non-polar phase as reference structure that has null polarization.

where we indicate with r_i^W the positions of the Wannier centers, with R_I (Z_I) the ionic positions (charges) and with V the volume of the system. For a periodic structure, P is defined modulo $2eR_l/V$, with R_l being a direct lattice vector.
In the previous formula (Eq. 5.1), if one divides by the number of ZnO pairs that compose the system instead of dividing by V, one gets a dipole averaged over the whole structure (<LD>) [78]: in the case of a nanowire, this is a quantity that contains both bulk and surface effects. More specifically, local contributions (Local Dipoles - LD) can be obtained by partitioning the WF set and ionic charges into neutral units (Zn-O couples) in such a way to obtain zero polarization for the reference bulk ZB phase structure [78]. In this approach, one may think of the electronic charge as being localized into point charges ($-q$) located at the wannier center (WC) associated with occupied band states in each unit cell. Thus the approach entails mapping a quantum mechanical system onto a classical system which consist of point charges. This partition scheme yields D_{ZnO} = -0.24 D/pair for bulk ZnO, and when normalized to the volume occupied by a ZnO couple, P = -0.03 C/m^2 is obtained in agreement with other computational techniques, such as Berry Phase [18, 129].
For a WZ structure elongated along the spontaneous polarization axis [0001], and free to contract or expand along the perpendicular axes, as in the case of NWs, the change in polarization can be written in terms of the piezoelectric constants and of the applied strain as:

$$P - P_\circ = 2e_{31}\epsilon_1 + e_{33}\epsilon_3 = (e_{33} - 2e_{31}\nu)\epsilon_3, \tag{5.2}$$

where P indicates the polarization for a strained structure, $P_\circ$ is the equilibrium structure polarization, e_{31} and e_{33} are the piezoelectric constants, ϵ_i are the strains along the three lattice directions and ν is the Poisson ratio. In this case, the appropriate quantity to describe the response to strain is the *effective* piezoelectric constant, $e_{33}^{eff} = (e_{33} - 2e_{31}\nu)$. In the case of a bulk system (or in the core part of a NW as shown later), multiplying equation 5.2 by the volume, V, occupied by a ZnO pair, and expressing V as a function of the strained lattice parameters, it is possible to write an analytical formula for the dependence of <LD> on the applied strain, ϵ_3:

$$< LD >= PV = (P_\circ + \epsilon_3(e_{33} - 2e_{31}\nu))V_0(1 - \epsilon_3\nu)^2(1 + \epsilon_3). \tag{5.3}$$

(V_0 is the equilibrium volume/ZnO pair, i.e. at zero strain)

With above Eq. 5.3, <LD> and P can be linked, thus we can compare results obtained using our approach with those obtained via other methods reported in literature.

5.3 Structural properties of ZnO NWs

In this study, we have considered ZnO NWs of increasing diameter in the range ≃4 Å to 23 Å which are represented in the insets of Fig. 5.1. Description of computational procedure and parameters used are presented in the Appendix A. These NWs have hexagonal shape (being made of N hexagonal shells, $N = 1, \ldots, 4$) and present non polar $(1\bar{1}00)$ facets, in agreement with experimental observation. At equilibrium geometry, two main relaxation mechanisms occur: The lattice parameter along the NW axis changes with respect to the bulk value and the atoms at the NW surfaces relax. The lattice constant c along the NW axis increases decreasing the NW diameter and, except for the smallest diameter NW1 ($N = 1$), the behavior appears to be linear. The anomalous behavior of the smallest NW is due to the fact that this NW has no bulk-like ZnO pairs: None of its atoms is four-fold coordinated. While the NWs elongate along the c direction, the lattice parameters along the perpendicular directions ($a = b$) shrink, since ZnO has a positive Poisson ratio ($\nu = -\epsilon_1/\epsilon_3$) for a strain applied along the c axis. The NW surfaces present a relaxation mechanism which is very similar to what observed for extended surfaces [77, 79]: oxygen atoms move outwards and the zinc atoms inwards, as shown in Fig. 5.1**(b)**. We find that the ZnO bonds at the surface are about 1.88 Å and thus they are shrunk of about 4.3 % with respect to bulk bond length; this bond deformation decays away from the surface and finally approaches zero at the core, in agreement with other studies in literature [77]. The charge rearrangement at the NW surfaces is also consistent with what observed for an infinite $(1\bar{1}00)$ surface: the HO orbital appears to be a surface state characterized by charge accumulation on the surface O atoms.

We have also evaluated the formation energy of the ZnO NWs (ΔE^{NW}) with increasing diameter defined as:

$$\Delta E^{NW} = E_T^{NW} - n\mu_{ZnO}^{bulk}. \tag{5.4}$$

where E^{NW} represents the total energy of the ZnO NW, n in the number of ZnO couples in the NW unit cell and μ_{ZnO}^{bulk} is the chemical potential of bulk ZnO in its stable phase (wurtzite structure). The calculated values of ΔE^{NW} are presented in Fig. 5.2. It is apparent that NWs formation energies are positive and as such they represent metastable ZnO structures. The formation energy decreases with increasing NW radius and it approaches the ZnO bulk value for vary large diameter due to the decrease of the surface/volume ratio.

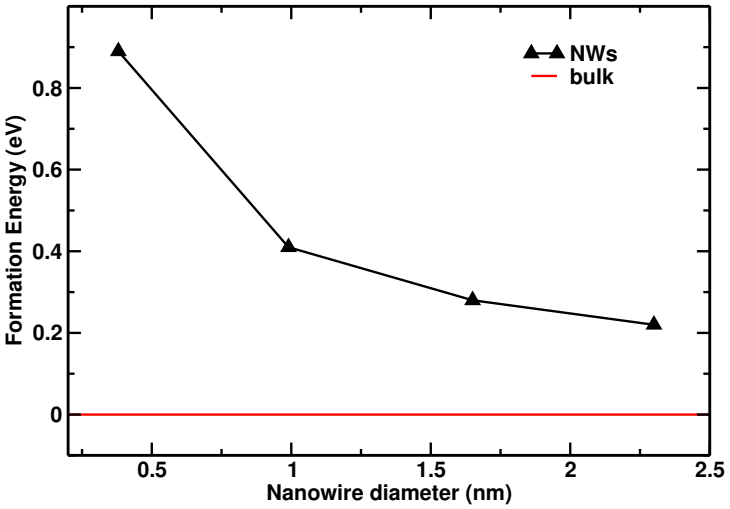

FIGURE 5.2: Formation energy for NWs with increasing diameter. The calculated bulk formation energy is set as the reference.

	Bulk	NW4	NW3	NW2	NW1
N	∞	4	3	2	1
$a[nm]$	3.289	3.280	3.276	3.269	3.274
c[Å]	5.315	5.361	5.385	5.423	5.397
d$[nm]$	∞	2.30	1.65	0.99	0.38
<LD>/Strain [D]	9.53	9.95	10.19	10.81	13.11
U$''$[eV]	30.75	22.37	21.94	19.44	15.94

TABLE 5.2: Structural, mechanical, and piezoelectric properties of ZnO in bulk and NWs form. N is the number hexagonal shells of the NWs, $d[nm]$ is the diameter of the ZnO NWs with atoms taken as point charge, c represents the lattice periodicity along the NW axis, <LD>/Strain is the rate change of average LD with respect to strain, and U'' is the effective strain energy (see equation 5.7).

5.4 Piezoelectric properties of ZnO NWs

As described before, the polar properties of a ZnO NWs has been studied in terms of LD. From a radial analysis of LDs, obtained by averaging LD contributions of ZnO pairs contained in concentric cylindrical shells at increasing distance from the NW center, one can see that for the largest wires considered in this study (NW3 and NW4), bulk behavior (<LD>=-0.24 D) is quickly recovered after the outermost shell, as shown in Fig. 5.3. In particular, for these two wires, one can clearly identify a core part in which ZnO pairs have bulk-like behavior (points of the flat region of Fig. 5.3) and a surface shell that strongly deviates from bulk-like behavior. In this way, one eliminates inconsistencies and arbitrariness linked to the common relations that use diameter or volume of the system: the scheme provides a method to define in an unambiguous and rigorous way a normalization useful in particular for nanostructures, although recovering bulk limits at

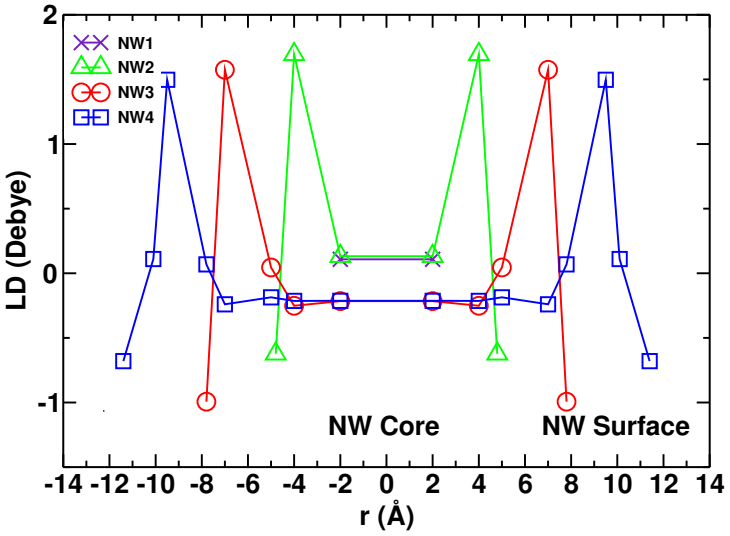

FIGURE 5.3: Radial LD analysis in NWs: each point represents the average LD in concentric cylindrical shells at increasing distance from the NW center located an the zero of the abscissa axis.

increasing size [78].

The piezoelectric response of the ZnO wires grown along the [0001] axis, which is also the direction of spontaneous polarization, was calculated in terms of variation of <LD> with respect to strain. The results for longitudinal strain (ϵ_3) ranging from -3% to 3% are reported in Fig. 5.4[**a**]. It is apparent that apart from the smallest wire, which structurally does not have any bulk-like ZnO pair, the behavior is well approximated by a linear fit whose slope is related to the piezoelectric response of the wire (see table 5.2). Also the analysis in terms of <LD>/strain reveals that NWs and bulk ZnO have similar piezoelectric behavior. Only NW1 is characterized by a fairly large increase of the slope, but this system is most probably unphysical. This close similarity between bulk and nanostructure piezoelectric responses reveals that the high enhancement of piezoelectric constants reported in Ref. [19] should not occur, and it is possibly related to different effects, other than the NW size. Taking advantage of the local analysis previously discussed, for NW3 and NW4 it is possible to separate the surface and core contribution to <LD> as a function of strain. The surface contribution is obtained by averaging LD on the ZnO pairs that deviate from bulk-like behavior and uniquely identified by the radial analysis reported in Fig. 5.3, while the core contribution is obtained by averaging over bulk-like inner ZnO shells (results are reported in panel [**c**] and panel [**b**] of Fig. 5.4 respectively). Interestingly, also the surface contribution to the wire response is almost linear and the values of <LD>/strain have values of 1.79 D and 1.25 D for NW3 and NW4 surfaces respectively (to be compared with the values reported in Table 5.2). This result indicates that the surface response to deformation is about one order of magnitude smaller than the bulk-like term and only slightly dependent on size; furthermore surface

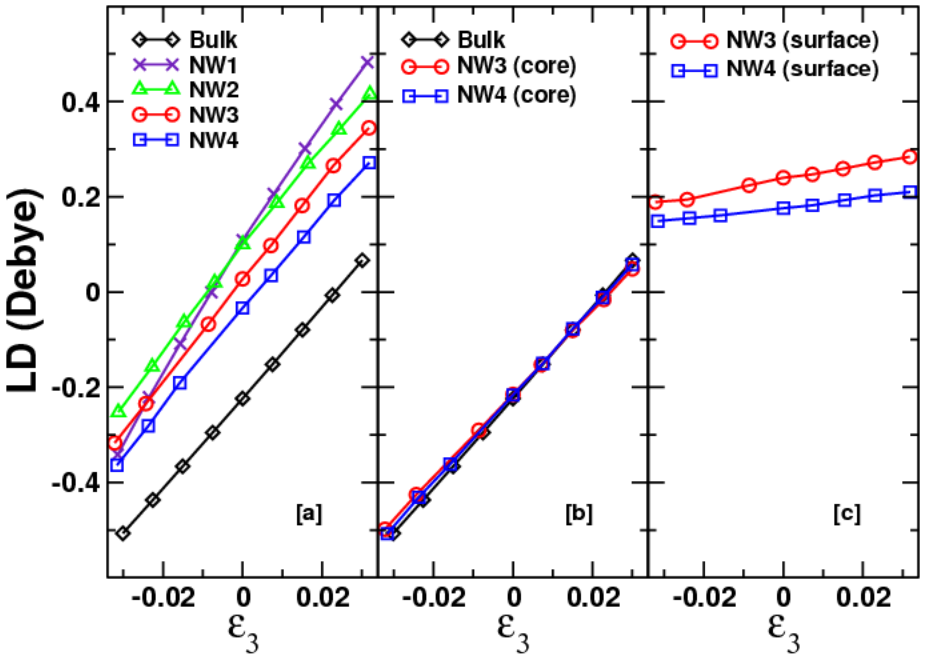

FIGURE 5.4: [a] Plot of <LD> *vs* strain (ϵ_3) for NWs with increasing diameter; [b] ([c]) represents the core (surface) contribution alone, for NW3 and NW4 compared to bulk.

contributions become quickly negligible and the surface/volume ratio decreases. These results are comparable to those reported in Ref. [18, 129], but significantly smaller than those reported in Ref. [19], probably due to the use of incorrect volume values in their calculated quantities.

We then use Eq. 5.3 to fit the data reported in Fig. 5.4(**b**) letting V_0, $P_\circ$, e_{31}, e_{33} and ν as free parameters. From the latter values it is possible to estimate e_{33}^{eff} for the wire cores: for NW3 and NW4 we obtain Poisson ratio, ν, values of 0.27 and 0.28, respectively that well compare to the value of 0.29 calculated for ZnO bulk. Correspondingly, the effective piezoelectric constant of NW3 and NW4 estimated in this way are 1.19 and 1.21 C/m^2 respectively, very close to the DFT bulk value of 1.28 C/m^2 (experimental 1.22 C/m^2[111]).

In order to verify the consistency of the analysis made in terms of LD with a more "classical" approach to polarization, we have analyzed how the displacement (d_z) of the ions in a ZnO bond change when a strain along the nanowire axis is applied (ϵ_3). In particular, we have analyzed how the $d_z(\epsilon)$ varies in a bulk system and in different portions of a nanowire (core vs shell). This quantity reflects only the ionic contribution to polarization, completely neglecting the electronic one, which is instead captured by

the analysis made in terms of wannier function, presented before. From an analysis of

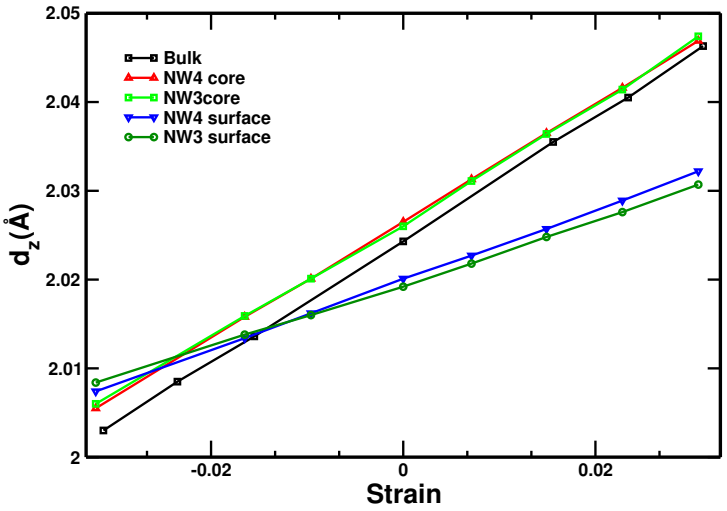

FIGURE 5.5: ZnO bond distance (dz) as a function of the applied strain for a bulk ZnO systems and for the core and surface portion of ZnO nanowires

Fig. 5.5 it is apparent that the core of the wires has a behavior close to the bulk one (the slope of the data are 0.69 Å for a ZnO bulk, 0.66 Å for NW4 and 0.65 Å for NW3). Moreover, comparing the curve characterizing the core and the surface of a wire, it is evident that, in the case of the surface layer, the slope is reduced by about 40% (0.39 Å for NW4 and 0.35 Å for NW3). In summary, also this analysis shows the bulk behavior is quickly recovered moving away from the surface already beyond the second ZnO layer from the surface.

In conclusion, bulk polar behavior is quickly recovered moving away from the surface and even in small nanowires the core part has a response to strain in terms of polarization that does not present enhancement effects. Furthermore, our analysis shows that piezoelectric constants expressed in terms of <LD> are negligibly influenced by the NW size. Surface effects and quantum confinement which are normally anticipated to dramatically modify properties of nanostructures seem to have minor influence especially on piezoelectric properties. Similar findings have been reported by Dai and co-workers [130], who, using DFT, showed that for thin films the piezoelectric constant converges rapidly with increase in film thickness, in contradiction with classical molecular dynamics results where slow convergence was predicted [19].

5.5 Mechanical properties of ZnO NWs

In order to explain the energy harvesting mechanism observed in ZnO NWs [14], and to describe why it is expected that nanostructures perform better than bulk systems, we analyzed how nanowires respond to external mechanical deformation and evaluated

their effective spring constants. In the elastic regime the strain energy, U, required to elongate the lattice parameter of a wire along its main axis of an amount Δc can be written as:

$$U(\Delta c) = \frac{1}{2}k\Delta c^2 = \frac{1}{2}k\Delta c^2(\frac{c_0}{c_0})^2 \tag{5.5}$$

$$= \frac{1}{2}kc_0^2\epsilon_3^2 = \frac{1}{2}K\epsilon_3^2 \tag{5.6}$$

where k is the elastic constant of the nanostructure, $K = kc_0^2$ is the effective spring constant, c_0 is the NW equilibrium lattice parameter and ϵ is the strain applied along the wire axis. From the above equations we obtain the strain energy per Zn-O pair, U_s:

$$U_s = \frac{U(\Delta c)}{n} = \frac{1}{2n}K\epsilon_3^2 = \frac{1}{2}U''\epsilon_3^2 \tag{5.7}$$

where n is the number of ZnO pairs in the simulation supercell and $U'' = \frac{K}{n}$ is called effective strain energy of the system. The latter quantity gives a quantitative estimate of the amount of energy required to deform a finite structure and contains both bulk and surface effects. As reported in table 5.2, the effective strain energy decreases with decreasing the size of the NWs, and for the smallest wire it is reduced of about 50%. Indeed, other studies have shown nanowires can sustain high deformation, thus can be repeatedly used for energy harvesting without breaking them [131].

The above results contribute to solve an existing debate on the mechanical properties of ZnO NWs still present in literature (see e.g. [15] and Refs therein), and support the conclusion that the Young's modulus of ZnO wires decreases with decreasing size. This information is relevant to open the way for the design and fabrication of efficient energy scavenging devices based on nanostructures. Furthermore, the results show that the energy requirements of these smart devices belong to the range of environmental noise, such as air, vibration, fluid flow and others [132].

Chapter 6

Ethanol gas sensing with ZnO NWs

This chapter deals with ethanol gas sensing by ZnO NWs with emphasis on the mechanism responsible for detection which is experimentally achieved by monitoring changes in electrical properties of the wires upon gas exposure. In particular, we employ first principles calculations to investigate how the electronic properties of ZnO($1\bar{1}00$) surfaces change when they interact with ethanol and oxygen, moreover intrinsic n-type doping typical on ZnO samples has been modelled by introducing interstitial hydrogen in the ZnO structure as discussed in Chapter 4. The electronic properties of the systems were studied at the GGA+U level, to cope with the well known band gap underestimation typical of GGA.

6.1 Introduction

As early as 1962, it was known that ZnO films could be used as gas sensors due to the fact that adsorption and desorption of gases cause change in ZnO electrical conductivity [22]. In particular, it was observed that at high temperature (about 400 °C) the adsorption and successive desorption process on the surface of ZnO was rapid enough to show a marked change in electrical conductivity. Since then, several critical issues related to ZnO gas sensing have been studies, such as, the role of catalyst [133], effects of additives [134], and significance of grain-size [135] amongst others.

Recent advances in growth techniques of ZnO nanostructures with different morphologies has lead to shift in interest to nanostructures due to their promising performance as gas sensors. Nanowires, defined as wires with at least one spatial dimension in the range of 1–100 nm [136], exhibit a variety of interesting and fascinating properties, and have been

functioning as building blocks for nanosensing technology [137, 138]. Although the basic gas sensing principle remains unchanged compared to the conventional sensors based on flat films, nanowire gas sensors and sensors arrays exhibit many inspiring characteristics:

- Ultra sensitivity and fast response time. Owing to their small size that ensures high surface-to-volume ratio, only a few gas molecules are sufficient to change the electrical properties of the sensing elements. This allows detection of very low concentration of gas within several seconds.
- Higher selectivity and stability. With the development of nanowire gas sensors, large arrays of macroscopic individual gas sensors can be replaced with a single device that integrates the sensing and signal processing functions in one chip, thus improved selectivity and stability can be achieved [139].
- Light weight, low power consumption and wireless communication capability. NW sensors having minimal size, light weight and consuming less power, are ideal for long range coverage [140], e.g. advanced gas sensor and wireless communication capabilities can be realized via distributed ad-hoc sensor networks, enabling long range guidance of all kinds of gas detection.
- Low-temperature operations. Very small amounts of gas can change the electrical characteristics of nanowires; this enables the sensors to work at lower-operating temperature. Single ZnO nanowires coated with Pt clusters by sputtering are shown to selectively detect hydrogen at room temperature, and operate at extremely low power levels of 15–30 W [141].

Usually, a nanocrystalline based layer deposited or grown among interdigitized electrodes is used in real experimental devices [4]. However, this device configuration prevents detailed studies and analysis from being carried out. Various difficulties exist for such configuration: Surfaces of the nano crystalline material can hide and disguise the molecules interactions and chemical surface reactions, also the complex network of grain boundaries existing in the nanocrystalline sensing material can cause charge transfer complexities. Furthermore, many basic analyses and studies, like surface analysis are experimentally performed far away from realistic operation conditions, i.e., in vacuum conditions for X-ray Photoelectron Spectroscope (XPS), High Resolution Transmission Microscopy (HRTEM), Electron Energy Loses Spectroscopy (EELS), or the use of higher gas concentration than usual for Fourier Transformed Infrared (FTIR) [8, 142], which again prevents reliable interpretation on the chemical to electrical transduction mechanisms. For this reason, new experimental and theoretical studies are needed to achieve better knowledge and understanding of the mechanism responsible for chemical to electrical transduction.

6.2 State of the art

The ability to detect ethanol gas is highly desirable as it is used in a variety of commercial products and industrial processes. Ethanol sensors based on ZnO nanostructures have been realized by a number of groups [4, 24–26], in all cases the conductivity of ZnO NWs increase when exposed to ethanol. The exact mechanism that cause a gas response is still not well understood; however, it is generally agreed that metal oxide based gas sensors rely on changes in electrical conductivity upon interaction with the surrounding atmosphere. Some studies have suggested that, when interacting with the ZnO surface at elevated temperature, ethanol undergoes a redox reaction and that it is the exchange of electrons with the substrate responsible for the change in ZnO conductivity. In particular, it has been proposed that ethanol can decompose following two different reaction paths, depending on the oxide[143]:

$$C_2H_5OH \rightarrow C_2H_4 + H_2O(acidic - oxide) \tag{6.1}$$

$$2C_2H_5OH \rightarrow 2CH_3CHO + H_2(basic - oxide) \tag{6.2}$$

Since ZnO is a basic oxide, the second of these two reactions (dehydrogenation) is favored. Other studies based on Temperature Programmed Desorption (TPD) [144] have shown that ethanol molecularly adsorbs on the ZnO surface, and dissociates into ethoxy and hydrogen as the temperature increases. This study claimed that ethoxy is adsorbed on oxygen vacancies or Zn^{2+} ion sites while hydrogen is adsorbed on lattice oxygen. The ethoxy adsorbed on the Zn^{2+} ion sites associates with atomic hydrogen and desorbs as ethanol from the surface, while ethoxy, that is adsorbed on oxygen vacancies, can be removed from the surface as ethylene through C–O scission and β-hydride elimination reaction at 523 K.

Based on other type of measurements, other models have been proposed to describe gas sensing mechanism of ZnO nanostructures [4, 24–26]; in particular some studies have evidenced that sensing occurs also at temperature for which no ethanol dissociation occurs. Since these measurements are not free from artifacts or ambiguous interpretation, theoretical studies would assist in the validation or development of a realistic unique model. However, past theoretical studies have been dedicated almost exclusively to providing fundamental understanding of surface/ethanol interaction [64, 145], with mechanism leading to ethanol sensing getting little attention.

6.3 Results and discussion

Here we examine the ZnO sensing mechanism for ethanol, and show that O_2 present in the atmosphere plays a major role during detection. Our conclusions are based on model systems consisting of ZnO($1\bar{1}00$) surfaces[1] doped with interstitial hydrogen, since it has been recently shown that hydrogen is unintentionally present in ZnO samples [114] and it acts as shallow donor, as already discussed in Chapter 4.
The electronic properties discussed throughout this chapter were calculated employing the GGA+U method [122, 146], with Hubbard U values of 12.0 eV for the Zn $3d$ orbitals and 6.5 eV for the oxygen $2p$ orbitals[80]. Finally, spin polarization was included in calculations involving oxygen molecule (more computational details can be found in the appendix).

6.3.1 Oxygen adsorption at the ZnO($1\bar{1}00$) surface

In ambient conditions, oxygen is one of the dominant gases and it has a tendency to interact with the surfaces of metal oxides. Application of ZnO in photocatalysis and gas sensing are routinely carried out in ambient environment, thus understanding the role of oxygen in these application is relevant for designing better devices. In this study, we found two adsorption configuration for the O_2 molecule on the ZnO($1\bar{1}00$) surface, as shown in Fig. 6.1. Initially, the O_2 molecule is placed 2.8 Å above the ZnO surface, such that there is minimal interaction between the surface and the molecule. Then, the system is relaxed to the minimum energy configuration. Two local minima were

	d(Zn–O)	d(O=O)	ΔE_{ads}	E_{gap}
On-top	2.16	1.27	-0.16	2.70
Bridging	2.18	1.29	-0.32	2.80

TABLE 6.1: Calculated structural parameters for the adsorption of oxygen on the ZnO(1-100) surface: distance between the surface and molecule (d(Zn–O_g)), oxygen molecule bond length (d(O=O)), adsorption energy (ΔE_{ads}), and band gap (E_{gap}).

found, an on-top configuration (see Fig. 6.1(**a**–**b**)), and a bridging configuration (shown in Fig. 6.1(**c-d**)). The on-top adsorption configuration is characterized by one oxygen atom of the O_2 molecule binding to a surface Zn, while in the case of the bridging configuration, both oxygen atoms of the O_2 molecule bind to two neighboring Zn atoms of the surface to form a bridging O_2 molecule. In the case of bridging configuration a stronger interaction is expected since both O atoms participate in bonding, and, as a result the O=O bond-length is elongated by 5% with respect to the free molecule (see

[1] In ZnO nanowires (10–10) surface is the most stable and abundant [104]

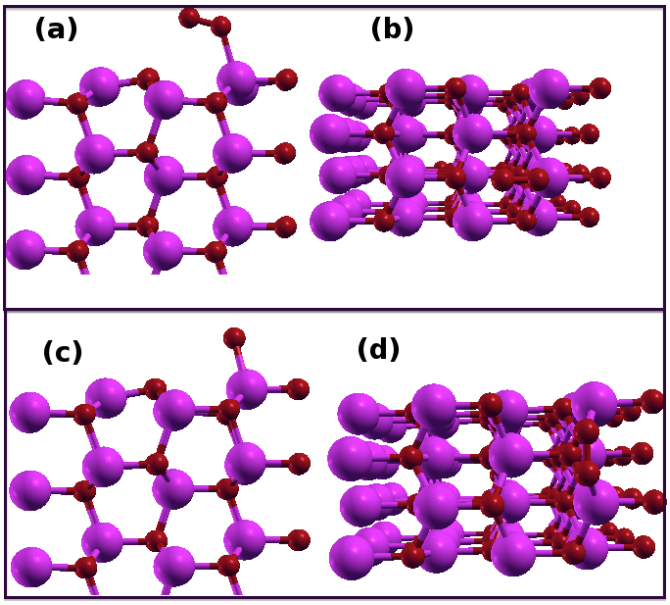

FIGURE 6.1: (**a**–**b**) Sideview and topview of oxygen molecule adsorbed in on-top configuration, (**c**–**d**) Sideview and topview of oxygen molecule adsorbed in bridging configuration.

Table 6.1).

The adsorption energy for these two configurations is determined by using Eq. 6.3 below,

$$\Delta E_{ads} = E_{bare+O_2} - E_{bare} - E_{O_2} \tag{6.3}$$

where E_{bare+O_2}, E_{bare}, and E_{O_2} are total energies of the surface with adsorbed an oxygen molecule, of the clean surface and of the oxygen molecule in a vacuum, respectively.

In both the on-top and bridging adsorption configurations a negative ΔE_{ads} was obtained, which clearly shows that these interaction are favored processes and can occur spontaneously in ambient conditions; however, the bridging configuration was found to be more energetically preferred due to its higher ΔE_{ads} of -0.32 eV. The total DOS for O_2 adsorbed on the ZnO surface is reported in Fig.6.2. Upon adsorption of an oxygen molecule, the Fermi level (E_F), which was located initially in CB (see Fig.4.2(**a**)), shifts back within the energy band-gap. signaling a reduction in conductivity, thus ZnO with adsorbed oxygen molecules becomes semi-conducting similar to the undoped system. The decrease in conductivity is attributed to the fact that when oxygen is adsorbed on the ZnO surface, it traps electron from the CB. This leads to a decrease of free electron carrier concentration and a decrease in conductivity, in agreement with experimental measurements performed in oxygen rich atmosphere [4, 61, 147].

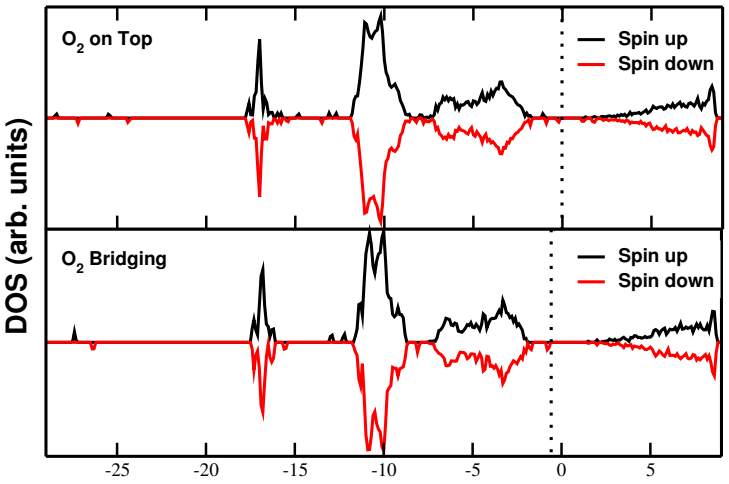

FIGURE 6.2: Density of state plots for [Top panel] On-top, and [bottom panel] bridging configuration of an oxygen molecule adsorbed on ZnO(1-100) surface. Dotted line show the location of Fermi level.

6.3.2 Ethanol adsorption on ZnO surface

We considered ethanol adsorption on the clean ZnO $(1\bar{1}00)$ surface of 1/4 ML surface coverage, as shown in Fig. 6.4. Initially, the ethanol molecule was placed 2.8 Å above the ZnO surface with the hydroxyl group (–OH) towards the ZnO surface. The system was then fully relaxed. In the minimum energy configuration, ethanol adsorbes

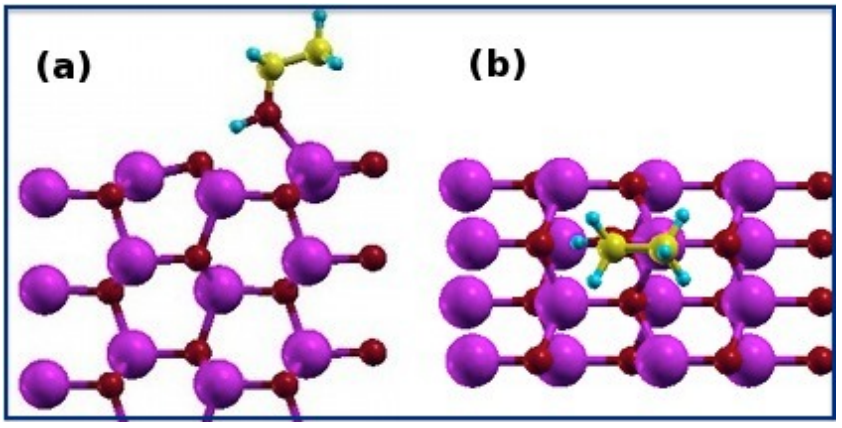

FIGURE 6.3: Ethanol adsorption on clean surface, (**a**) side view, and (**b**) topview of minimum energy configuration. Blue and yellow spheres represent hydrogen and carbon atoms, respectively.

through the hydroxyl group (–OH) forming a bridging configuration. In particular, the oxygen(hydrogen) of the hydroxyl binds to the surface Zn(O) with bond-length of 2.05 Å(1.56 Å), in agreement with previous theoretical studies [145, 148]. This configuration has an adsorption energy of -0.92 eV, which is characteristic of chemisorption interaction. Our results compare well with those of Spencer *et al.*[148] who obtained adsorption energy of 1.09 eV. Adsorption of ethanol on hydrogen doped surface does not signifi-

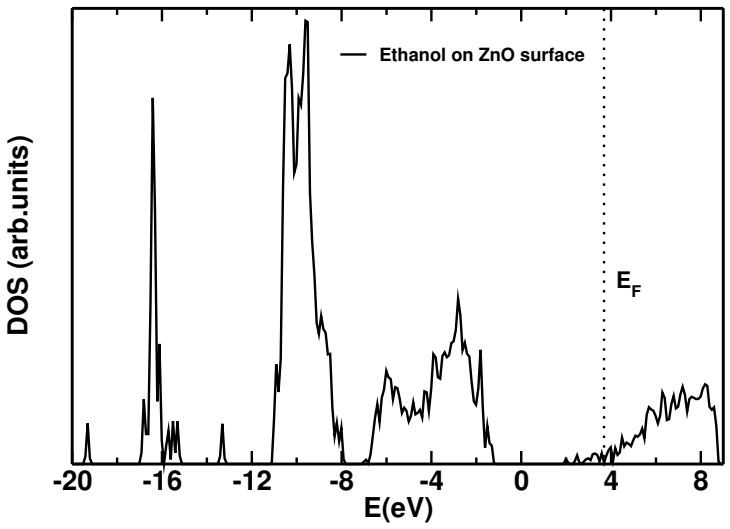

FIGURE 6.4: DOS plot for ethanol molecule adsorbed on stoichiometric ZnO surfaces with interstitial hydrogen. Dotted line show the location of Fermi level.

cantly affect ZnO electrical properties i.e., the location of E_F remain almost identical to that of the clean surface doped with hydrogen, as shown in Fig. 6.4. This shows that the quantity of free electrons in the CB does not change upon ethanol adsorption, hence ethanol alone is not responsible for the increase in ZnO conductivity as claimed in literature [148, 149].

6.3.3 Sensing mechanism

In the experimental set-up, gas detection is usually achieved by conductometric measurement that are based on the principle that adsorption or desorption of gases on sensor surface causes a change in conductivity. The sensing mechanism, however, can be very complicated. For example, depending on temperature, it has been shown that oxygen from the atmosphere may react with the oxide surface to form O^{2-}, O^{-}, and O_2^{-} ions, thus deterring this mechanism is not a straight forward exercise.

We have shown how surface electrical properties are modified when oxygen or ethanol is adsorbed on ZnO surfaces, and with this information we can describe how ethanol gas sensing is realized using ZnO. When pristine n-type ZnO NWs are exposed to ambient condition, which is normally rich in oxygen gas, their surfaces are immediately covered by O_2^{-} species because adsorbed oxygen would capture electrons from the CB, hence reducing free carrier density. When ethanol is introduced in the atmosphere, increased conductivity is observed. This is attributed to the fact that ethanol has higher adsorption energy compared to oxygen, hence it is able to remove oxygen from the surface, thus freeing trapped electrons which are injected back to CB, leading to increased surface conductivity. Therefore, electron carrier density would be closely linked to the concen-

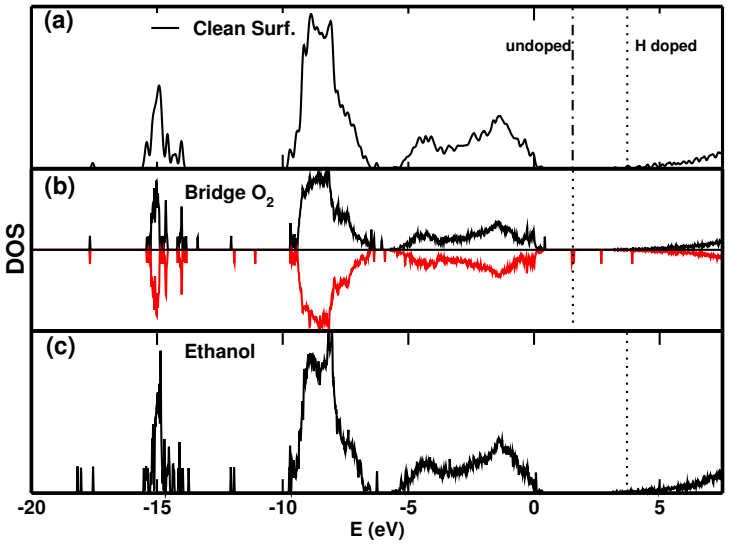

FIGURE 6.5: Density of state plots for (a) undoped and hydrogen doped ZnO surface, (b) oxygen molecule adsorption, and (c) ethanol molecule adsorption. Oxygen and ethanol molecules are adsorbed on stoichiometric ZnO surfaces doped with hydrogen, and the Dotted line show the location of Fermi level.

tration of ethanol in the atmosphere, such that higher conductivities can be attained when O_2^- ions are completely removed from the surface.

We can describe ethanol sensing mechanism as involving competitive adsorption occurring on the surface, with ethanol being able to remove pre-adsorbed oxygen molecules leading to enhanced conductivity, contrary to the usual models where ethanol is treated as reductive gas [4, 150, 151].

Chapter 7

Formation, distribution, and control of oxygen vacancies in ZnO nano-structures

Native or intrinsic defects are imperfections in the crystal lattice that involve only the constituent elements [152]. They include vacancies (missing atoms at regular lattice positions), interstitials (extra atoms occupying interstices in the lattice) and antisites (a Zn atom occupying an O lattice site or vice versa). In literature, studies have show that oxygen vacancies influence some of the applications of ZnO. For example, oxygen vacancies play a role in catalytic activity as well as optical application of ZnO [153, 154]. Furthermore, oxygen vacancies are considered to be crucial in ZnO doping, and are also involved in the diffusion mechanisms connected to growth, device processing and degradation [103]. Understanding the incorporation and behavior of oxygen vacancies in ZnO is essential for its successful application in semiconductor industry.

Diffusion experiments provide information on atomic migration as well as the general defect chemistry of a system [155]. The interpretation of diffusion experiments are often difficult and defect properties are obtained from indirect measurement, hence prone to errors and misinterpretation. Indeed several experimental studies focussed on the determination of defect diffusion coefficients [156–162] show a large scatter in the data, thus no consensus has been reached on activation energies, exponential pre-factors, or migration mechanisms. Therefore, a systematic theoretical investigation is highly desirable in order to obtain more fundamental insights on the subject. Hitherto, theoretical investigations based on quantum-mechanical calculations have been conducted to explore static properties of intrinsic as well as extrinsic point defects in ZnO (see e.g., Refs. [6, 32, 163, 164]). Recently, migration barriers were calculated for Li in wurtzitic ZnO [162] and for the doubly positively charged zinc interstitial in cubic ZnO (zinc blende

structure) [165], but at present there is no comprehensive study on the mobilities of intrinsic point defects in zinc oxide.
Furthermore, distribution and concentration of oxygen vacancies at the surface of ZnO nanostructures is still not well understood. For instance, Vlasenko *et al.* [30] reported noticeable concentration of oxygen vacancies in as-grown ZnO only after electron irradiation, while Selim *et al.* [31] on the other hand found high concentration in as grown ZnO detectable even without need of irradiation. Similar inconsistencies have been reported also in theoretical work [32–34].

7.1 Computational details

For the defect calculations we used hexagonal supercells with 96 atoms that is equivalent to (2×2) lateral periodicity of primitive unit cells. In these calculations a shifted k-point 4×4×1 mesh was employed, and all calculations were performed within GGA as described in Appendix A.
In order to determine migration paths and barrier energies for oxygen vacancy in ZnO, DFT calculations combined with Climbing Image Nudged Elastic Bands (CI-NEB) [102] were performed considering diffusion path orthogonal to the surface. This is the most probable route for in/out of surface diffusion [6], as shown in Fig. 7.2.
CI-NEB method allows minimal number of constraints to be imposed when searching for saddle points, and unlike experiments which provide only an average value for the diffusivity, the present approach allows to separate unequivocally the various contributions to the diffusivity, thus better insights can be gained. The relevant quantities are schematically depicted for a one-dimensional potential energy surface (PES) in Fig. 7.1(**a**). Local minima can be determined with comparably small computational effort i.e., conjugated gradients minimization, Monte-Carlo techniques or simulated annealing. The identification of minimum energy paths (MEP) and thus energy barriers constitutes a more difficult task, and is routinely determined by NEB approach. In the NEB method [166] a number of images are distributed between the initial (e.g., vacancy on site A) and the final state (e.g., vacancy on site B) of the system, as shown in Fig. 7.2. The images are connected via elastic springs. A numerical algorithm (e.g., conjugated gradients or damped molecular dynamics) is used to minimize the forces on the images by taking into account the action of the springs. Upon optimization, the chain of images successively moves towards the nearest MEP. The situation is schematically shown for a two-dimensional PES in Fig. 7.1(**b**).
The CI-NEB scheme is an extension of the standard NEB method [102]. Firstly, the image with the highest energy is selected. Then the force along the direction of the two

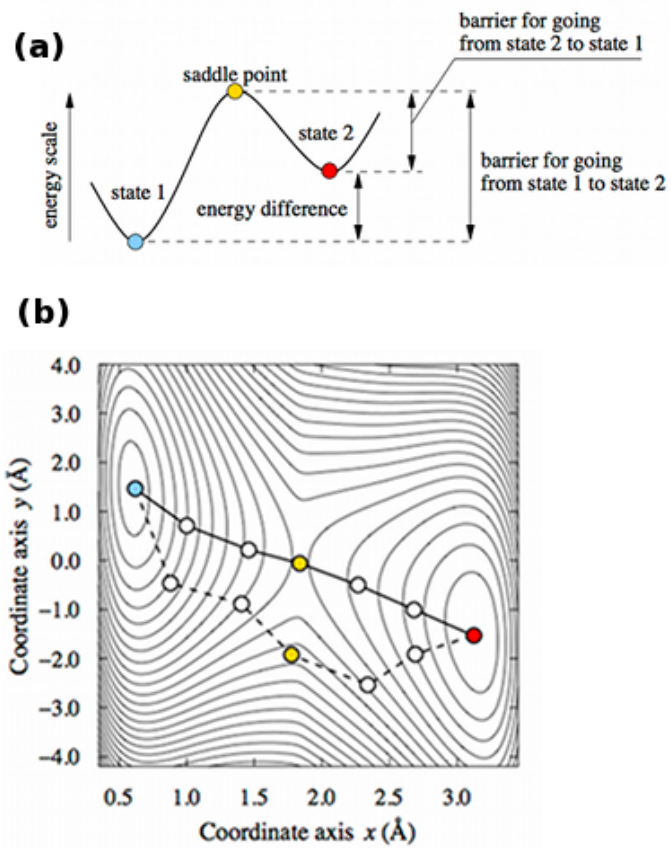

FIGURE 7.1: (a) Schematic of a one-dimensional potential energy surface, (b) Schematic of a two-dimensional potential energy surface illustrating the NEB/CI-NEB method. The blue and red circles mark the initial and final state respectively. The dashed and solid lines show the NEB at the beginning and the end of the optimization. The white circles mark intermediate images of the system. The yellow circles indicate the climbing image which is the replica with the highest energy and which eventually is located at the saddle point [6].

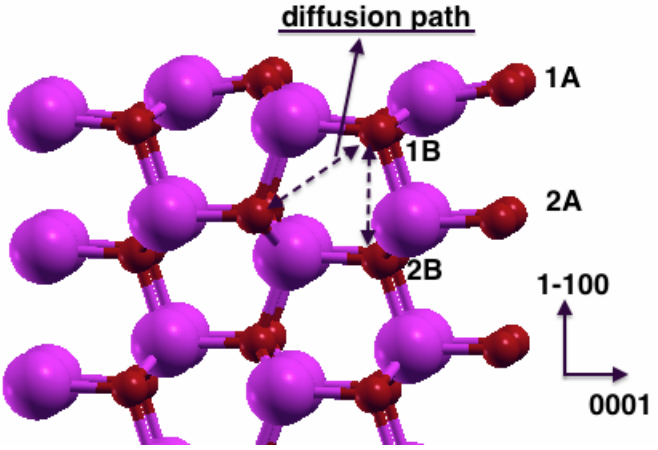

FIGURE 7.2: Graphical representation of diffusion path of oxygen vacancies via jumps to first nearest oxygen site and the arrow shows the paths considered in the study, and the purple (red) sphere represent Zn(O) atoms.

neighboring images is projected out and inverted. Eventually, all forces are minimized. When convergence is achieved, the climbing image is located at the saddle point.

7.2 Formation of oxygen vacancies

The formation energy of a defect or impurity as well as their concentration can be computed entirely from first principles, without resorting to experimental data. Density-functional theory allowed us to calculate the ground-state total energy of systems of electrons subject to an external potential, i.e. the Coulomb potential given by the nuclei or ions. From total energies one can easily compute the formation energy of defects, as described in these Refs. [167–169]. First-principles density- functional calculations of defects in solids are nowadays performed using supercells containing up to several 100 atoms, periodically repeated in the three-dimensional space. The supercell size should be large enough to simulate isolated defects, i.e. the interactions between defects in neighboring supercells should be negligible.

7.2.1 Structural properties

In our study, we consider a surface that consist of 12 layers of ZnO, which has been shown to be sufficient for simulating surfaces [79]. In this configuration, oxygen vacancies are introduced on the surface with a concentration of 1/4 of monolayer coverage, and the distance between neighboring oxygen vacancies was large enough to consider the vacancies as effectively isolated. DFT calculation based on GGA-PBE described in Appendix A was employed in the study, and the oxygen vacancies were introduced as a function of distance from the surface.

As far as the structural properties are concerned, the presence of a vacancy in the topmost layer induces an inward displacement of the unpaired Zn atom so as to restore a bulk-like 4-fold coordination with the two neighbor Zn atoms of the second layer (see Fig. 7.3(**a**)), in agreement with previous studies [79, 170, 171]. Significant relaxation effects are also observed when the vacancy is located in the first two subsurface layers, however, for oxygen vacancies located in deeper layers, relaxation effects are more moderate and very similar to those observed in the defected bulk crystal. Moreover, the vacancy-induced distortions are mostly localized around the defect, whereas the geometry of the stoichiometric system is almost preserved in the regions far from the defect site.

As mentioned before, oxygen vacancies influence some of the application of ZnO based devices, thus the knowledge of defect concentration and distribution in such surfaces is important. The vacancy formation energy, which is a measure of energy required

to remove an oxygen atom from the stoichiometric surface, have been calculated as a function of the vacancy position with respect to the surface, as shown below,

$$E^f = E_d - E_{st} + N_{vac} \times \frac{1}{2} E_{O_2} \tag{7.1}$$

where E_d, E_{clean}, and E_{O_2} are DFT total energies of defected surface, stoichiometric slab, and spin polarized oxygen molecule calculated in vacuum, respectively.

Oxygen vacancies located on the surface have lower E^f ($\sim$ 2.81 eV) compared to those

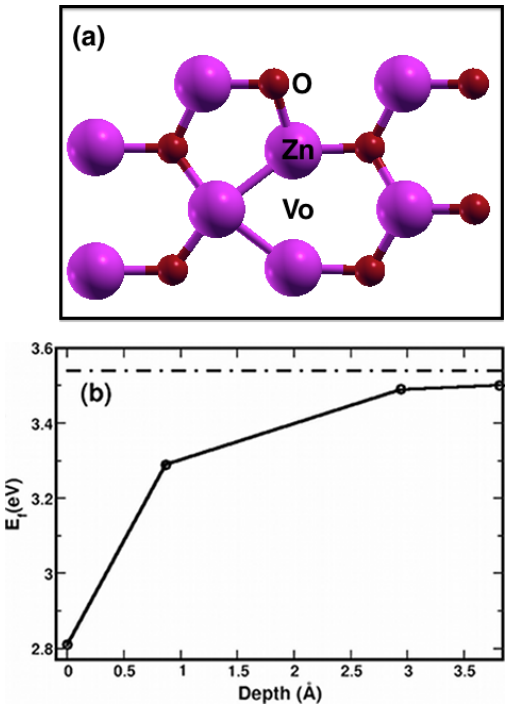

FIGURE 7.3: (a) Topview of relaxed $1\bar{1}00$ surface with oxygen vacancy, (b) profile of oxygen vacancy formation energy where vacancy located on the surface correspond to 0 Å depth and the dashed line shows vacancy formation energy in bulk.

located in subsurface region (3.29 eV), and bulk limit is approached in deeper layer, as shown in Fig. 7.3(**b**). Therefore, oxygen vacancies are more likely to form on the surface compared to deeper layers due to lower formation energies; most With the knowledge of oxygen vacancy formation energy, it is possible to evaluate their concentration using rate equation (Eq. 7.2). In thermodynamic equilibrium, defect concentration (C) is quantitatively determined using rate equation shown below,

$$C = N_{vac} \exp\left(\frac{-E_f}{K_B T}\right). \tag{7.2}$$

where N_{vac} is number of vacancy sites per unit volume in the simulation cell, K_B is the Boltzmann constant, and T is the temperature. A low formation energy implies a high equilibrium concentration of the defects, whereas a high formation energy means that

defects are unlikely to occur. We further find that the formation energy of an oxygen vacancy in the ZnO surface is about 0.775 eV lower than that in the ZnO bulk. This indicates that oxygen vacancies can form even more easily in ZnO (10–10) surfaces than in ZnO bulk. Although, the actual defect concentration may depend of the exchange and correlation functional employed in the DFT calculations, the qualitative picture of vacancy accumulation at surface would still hold. Indeed, the difference in bulk versus surface defect formation energy is much larger than the dependence of the defect formation energies on the functional [8].

7.2.2 Electronic properties

The character of the near-gap states can be inferred from the analysis of the projected density of states (PDOS) on atomic orbitals, as shown in Fig. 7.4(**a**). In the surfaces, the top valence band is mainly derived from the p orbitals of O atoms with Zn atoms giving negligible contribution. On the other hand, the bottom conduction band is strongly dominated by the bulk contributions in agreement with recent first- principles studies [171, 172]. The presence of the defects is responsible for the appearance of detects

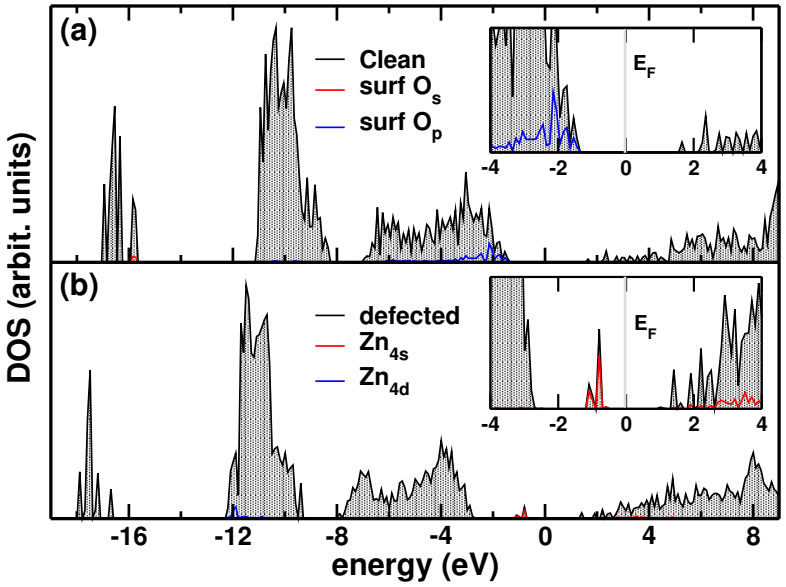

FIGURE 7.4: Total and projected density of states for (a) clean, (b) defected surface. The insets show a zoom in proximity of the band gap.

states which are located about 2 eV above top valence band. Such states, as revealed by the PDOS analysis (see Fig. 7.4(**b**)), are mainly derived from the Zn_{4s} atomic orbitals belonging to Zn atoms surrounding the vacancy. The calculated distance of defect state from CB as a function of the vacancy depth from the surface are reported in Table. 7.1. The distance of defect state from CB is strongly influenced by the hybridization of the atomic orbitals surrounding the vacancy, which explains its dependence on the vacancy

Depth ($\AA$)	0.0	0.8	2.9	3.5
Distance of defect state from the CB	1.8	1.9	2.2	2.3

TABLE 7.1: Bandgap calculated using GGA+U for oxygen vacancy located at varied depth from the surface.

site. In particular, a moderate dependence on the depth is found for oxygen vacancies, similar results have been reported elsewhere [171].

7.3 Oxygen vacancy diffusion

Barrier energy (E_b) is the minimum energy that must be input to a chemical system, containing potential reactants, in order for a chemical reaction to occur. Once E_b is known, the process rate can be easily determined using the expression $\Gamma = \Gamma_o \exp(-E_b/k_B T)$ [171], where the prefactor Γ_o is the ratio of the vibrational frequencies at the initial configuration to the frequencies at the saddle point (see Fig. 7.1(**a**)); k_B is the Boltzmann constant; and T is the temperature. A reasonable estimate of the temperature at which the oxygen vacancy becomes mobile can be obtained by taking the definition of the activation temperature, i.e., the temperature at which the jump rate Γ is 1 s^{-1}. To a good approximation, Γ_o can be taken as a typical phonon frequency, i.e., 1013 s^{-1} [171]. Therefore, we can use $\Gamma = 1$ s $^{-1}$, $\Gamma_o = 1013$ s^{-1}, and the calculated E_b values for each path to estimate the annealing temperature, shown in Table 7.2.

TABLE 7.2: Calculated barrier energy (E_b) and estimated anneal ing temperature (T_a) for the oxygen vacancy diffusion between first neighbours following path shown in Fig. 7.2. Arrow has been used to show diffusion direction of the oxygen vacancy.

diffusion path	E_b(eV)		T_a (K)	
	direct	inverse	direct	inverse
$V_{O,1A} \rightarrow V_{O,2A}$	1.92	1.23	744	477
	1.90[a]	1.24[a]	737[a]	481[a]
$V_{O,1B} \rightarrow V_{O,2B}$	2.07	1.76	802	682
$V_{O,2B} \rightarrow V_{O,2B}$)	2.14	2.04	830	790
Bulk	2.23, 2.00[a]	2.23	428	428
	2.36[b]			

[a] Ref. [171]

[b] Ref. [173]

From our study, we obtain lower E_b for subsurface to surface diffusion of oxygen vacancies, which indicate the ease for vacancies to diffuse to the surface and is activated at

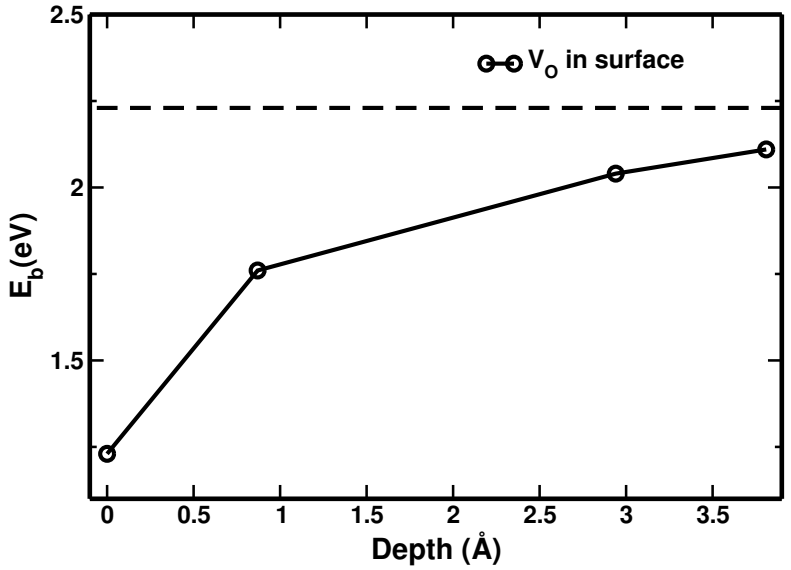

FIGURE 7.5: Barrier energy for oxygen vacancy diffusion into and out of the surface. Surface oxygen vacancy correspond to 0 Å depth with the dashed line showing the bulk limit.

moderate temperature of about 480 K. On the other hand, large value of E_b was obtained for surface to deep layer diffusion, thus suggesting that oxygen vacancies migration from surface to deeper layers is largely inhibited and unlikely to occur.

Our results compares well with previous studies, in particular, the bulk values that have been reported (see Table 7.2) shows reasonable agreement with our work, thus validating the oxygen vacancy prediction in surface and subsurface region that is not well documented in literature.

From this section, we can conclude that oxygen vacancies are likely to be formed on the surface of ZnO, and even if some may be formed in bulklike region of the nanostructure diffusion profile shows it will migrate to the surface when sufficient energy is supplied to overcome migration barrier i.e. when annealed.

7.4 Control of oxygen vacancies

Recent research has shown that the catalytic activity of ZnO is only indirectly related to the surface area; in fact it depends on the density of active sites [174]. For example, according to recent studies on methanol synthesis on ZnO surface [175], oxygen vacancies formed on the surface of ZnO crystals served as the active sites. Furthermore, recent studies have shown that oxygen vacancies are instrumental in the realization of p-type doping in ZnO [168, 176], also oxygen vacancies are essential for NO_2 gas sensing with ZnO by acting as adsorption sites [145, 177].

Previous studies have shown that oxygen vacancy rich ZnO NWs can be grown using chemical deposition technique with mixed ZnO and ZnS powder, and with sulfur acting as reducing agent. Indeed, photoluminescence measurements confirmed presence of intense green emission that is normally associated with oxygen vacancies. It is claimed that abundant generation of oxygen vacancies on the surface of ZnO NW was due to competition between ZnO and SO_2 for oxidation [178].
In this section, results of *ab initio* studies performed to give a microscopic understanding on the role of reducing agent, in this case sulphur or carbon in controlling the formation of oxygen vacancies is presented.

7.4.1 Structural properties

In our study, CO molecule was introduced 2.5 $\mathring{A}$ above the surface and perpendicular to oxygen atom on the surface. Both C-down and O-down orientation were considered, and it was found that the surface area in the vicinity of the topmost O ion was purely repulsive interaction for both cases of O and C atoms are and were repelled from the surface. On the other hand, both C-down and O-down showed enhanced interaction when introduced perpendicular to topmost Zn ion, and C-down orientation was found interact more favorably compared to O-down orientation, in agreement with experimental observation [179]. The data is presented in Table 7.3.

TABLE 7.3: Calculated distance between surface ions and adsorbed molecule ($d_o(\mathring{A})$), bond length of adsorbed molecule, and adsorption energies (E_{ad} (eV))

Orient	$d_o(\mathring{A})$	SO/CO $\mathring{A}$	E_{ad} (eV)
ZnO(Zn)C-down	2.18	1.14	-0.29, -0.36[a], -0.24[b]
ZnO(Zn)O-down	2.36	1.14	-0.10
ZnO(Zn)O-down	2.33	1.40	-0.23
ZnO(Zn)S-down	2.36	1.43	-0.50
Zn(O)S-down	1.70	1.65	-1.70

[a] Ref. [179]

[b] Ref. [180]

Therefore, we can conclude that for the case of CO interaction with ZnO surface, Zn–C bonding is the most probable interaction to be anticipated, thus suggesting that CO would act as a dopant. Similarly, experimental measurements based on Raman spectroscopy have indicated the presence of lattice defects and Zn–C type of complexes in the nano-crystalline carbon doped ZnO matrix, and is thought to be responsible for the enhancement of ferromagnetism in ZnO nanostructures [181, 182].
In the case of SO adsorption on ZnO surface, both O-down and S-down orientation were found to have negative adsorption energies, which shows these are favored interactions.

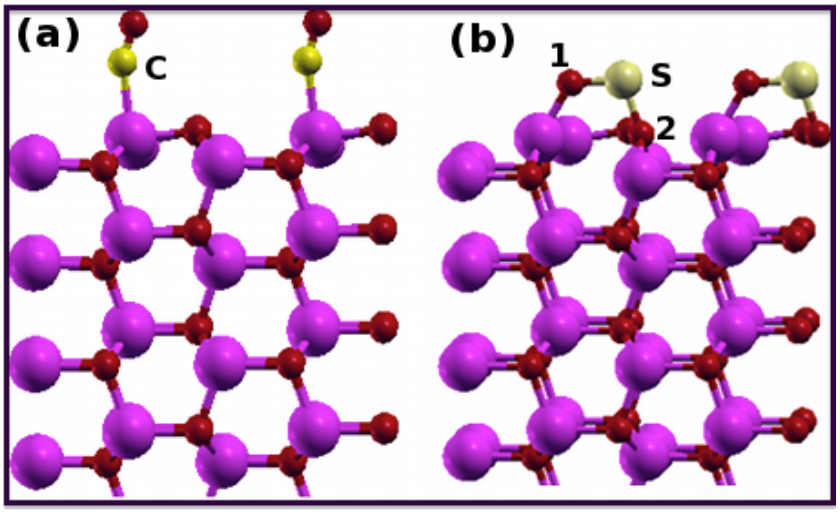

FIGURE 7.6: Schematic representation of preferred configuration for (a) CO, and (b) SO adsorption on ZnO surface. The red and purple spheres represent O, and Zn atom, respectively. The small yellow sphere in panel (a) is carbon, while the large yellow sphere in panel (b) represent sulphur atom.

On the other hand, O-down configuration on surface oxygen atom showed negligible interaction, while it was more preferred on Zn as demonstrated by higher adsorption energy.

S-down adsorption orientation had a more robust interaction on both Zn and O top-most surface ions; however, adsorption on surface O ion was more energetically preferred and is characterized by elongation of S–O bond to form SO_2, with both bondlength of O_1–S and S–O_2 being 1.65 $\AA$ and 1.7 $\AA$, respectively. The S–O bondlength obtained in this work is comparable to experimental value of 1.4 $\AA$ [178], as shown in Fig. 7.6(**b**), and the slight difference is attributed to GGA method which is know to overestimate bondlength.

7.4.2 SO_2 removal from ZnO surface

In the previous section, we have shown that sulphur can be used to induce Zn rich environment during growth of ZnO NWs by capturing oxygen to form SO_2, which is an important step in the creation of oxygen vacancies. Using CI-NEB described in the previous chapter, we explore the removal of SO_2 from the surface such that a vacancy is left behind, thus formation of vacancies, as described by Seo et al. [178].

In order to estimate the energies involved in removal of SO_2 from the surface, we consider SO_2 adsorbed on ZnO surface shown in Fig. 7.6(**b**) as the initial state, while the final state is a position where SO_2 is at least 3.0 $\AA$ away from the surface.

In order to remove SO_2 from the surface, an energy barrier of 0.63 eV has to be overcome, as shown in Fig. 7.7. It should be recalled that CI-NEB calculations are performed for

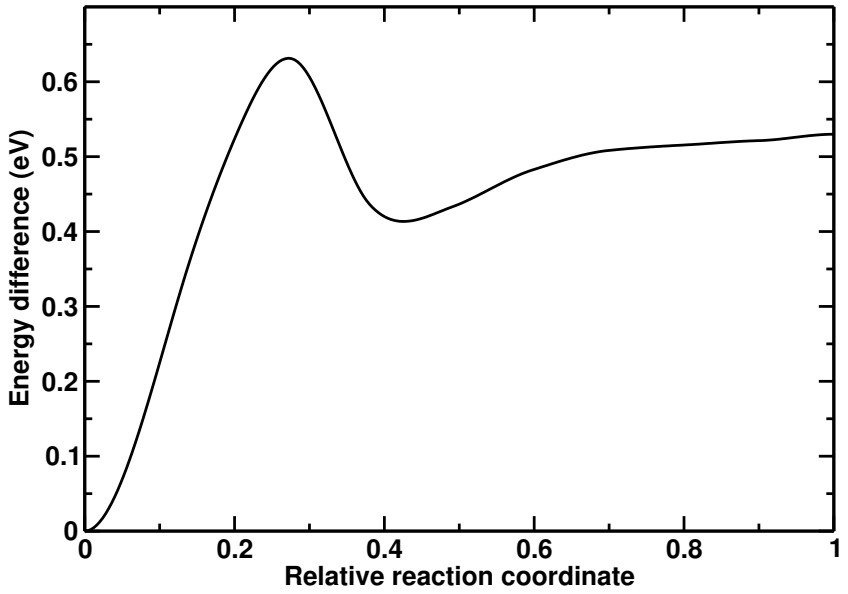

FIGURE 7.7: Energy pathway of SO_2 for removal from the surface, 0 coordinate correspond to SO configuration shown in Fig. 7.6(**b**), while 1 correspond to SO_2 at a distance from the surface.

a system at zero temperature, however growth condition occur at elevated temperatures of about 700 °C [178]. Indeed, ab initio molecular dynamic calculations showed that SO_2 get detached from the surface at sufficiently high temperatures of about 700 K. This clearly shows that sulphur can introduce oxygen vacancies on surfaces of ZnO in a controlled manner. Our theoretical study validates experimental study of Seo *et al.*[178] that have shown that sulphur can be used to form oxygen vacancies.

7.5 Discussion

ZnO NWs synthesized in Zn rich atmosphere favour formation of oxygen vacancies to occur in high concentration, and this has been confirmed by experimental measurement where strong green emission that is associate with oxygen vacancies was reported [30, 183], and when annealed at high temperature ($\sim$ 800 °C) the intensity of green emission decreased dramatically, which signals reduction of oxygen vacancies. From our study, we can interpret this behaviour as follows: as grown ZnO NWs have majority of oxygen vacancies located near the surface region. When exposed to ambient conditions, vacancies are filled almost immediately, while those in subsurface diffuse to the surface since ambient temperature can supply sufficient energy to activate migration and are filled once on the surface. In the case of large nanostructures that consist of bulk like cores and surface region annealed at high temperature oxygen vacancies in deep layers gain sufficient energy to overcome the migration barrier, thus diffuse to surface. This

leads to a decrease in concentration of oxygen vacancies, consistent with above experimental observation.

Chapter 8

Conclusion

The present dissertation combines Quantum Mechanical simulations based on Density Functional Theory, including Wanner Functions and Climbing Image-Nudged Elastic Band methods, with Thermodynamic concepts to elucidate energy harvesting and sensing capabilities of ZnO surface and nanostructures. The complexity of the experimental setup and demand, the non-standard characterization techniques, and the controversial theoretical studies existing in the field, still call for a consistent, unified description of the nanostructure response. In the first part of this work, using ab initio Density Functional Theory combined with Wannier functions, piezoelectric characterization of ZnO nanowires is performed. Our results reveal that piezoelectric coefficients of ZnO nanowires are independent of size effects, at least for most common NWs diameters: indeed, we have shown that wires whose diameter is more than 1.6 nm have piezoelectric coefficient similar to that of bulk ZnO. Our results reveal that the huge piezoelectric enhancement reported in previous studies is due to approximations that are valid to bulk systems, and appear to be ill defined quantities for nanostructures. To understand the reason behind the successful use of ZnO nanowires in energy scavenging and other related application, we studied their mechanical properties. It is revealed that effective strain energies of nanowires are more sensitive to size reduction and are much lower compared to bulk. Therefore, our theoretical predictions indicate that the advantage of using nanowires for energy harvesting is due to their sensitivity to small mechanical agitation: this knowledge may help in designing more efficient nanogenerators.
In order to understand the sensing mechanism of ethanol on ZnO surface, the energetic of oxygen and ethanol gases adsorption on the surface are studied separately and compared. In n-type material, as obtained for instance in the presence of hydrogen interstitial in ZnO, our results reveal that adsorption of oxygen on the surface is responsible for reduced conductivity as it traps electrons from conduction band, thus reduced

carrier concentration. On the other hand, ethanol adsorption on the surface have negligible effects on the electronic properties, in particular, the location of the Fermi level remains unchanged when compared to that of the clean surface. However, ethanol has an adsorption energy that is three times higher than that of oxygen gas, and is able to remove pre-adsorbed oxygen from the surface. We have interpreted this result in terms of competitive adsorption between oxygen and ethanol: since ethanol has higher adsorption energy on ZnO surfaces, it is able to remove pre-adsorbed oxygen, resulting in improved conductivity. This result, associated with release of trapped elecrons in conduction band, is consistent and explains the experimental observation that relates changes in conductivity upon ethanol exposure

Previous studies on intrinsic defects focussed mainly on bulk system, however defects near the surfaces region have received little attention yet are responsible for influencing performance of device based on ZnO. In the present work, combined density functional theory and climbing image nudged elastic band are used to study formation and distribution trends of oxygen vacancies. It is revealed that oxygen vacancies occur on the surface at 0 K: since growth occurs at elevated temperatures oxygen vacancy is possible, thus diffusion profile is studied, and it is revealed that oxygen vacancies experience low diffusion barrier in the case of deep layer to surface diffusion. Therefore, high mobility to the surface is predicted and better stoichiometry is expected in deeper layers of the surface.

In summary, the present study contributes to the understanding of the electromechanical properties of ZnO nanowires, gas sensing mechanism and formation trends of oxygen vacancies near the surface region of ZnO. These results provide basis for the interpretation and reinterpretation of experiments, which may be instrumental in development and optimization of devices for energy harvesting and gas sensing application.

Appendix A

Additional information

A.1 Computational details

All DFT calculation presented in this dissertation were performed with Quantum Espresso suite. In the case of nanowires, calculations were performed with reference to the theoretical DFT equilibrium lattice parameters of the ZnO wires (see Ref. [78]), using the ultrasoft pseudopotential plane wave implementation of DFT, with energy cutoff of 28 Ry (280 Ry) for the wavefunctions (charge density). The exchange-correlation energies were calculated by using the Perdew-Burke-Ernzerhof [109] approximation of the generalized gradient approach. Wannier functions for ZnO bulk and nanowires were evaluated using the wanT [184] code.
The nanowires were modeled in periodic supercells with the z direction corresponding to the wire axis (equilibium c lattice constants are reported in table 5.2), and lateral lattice parameters (along the x and y axes) large enough to avoid interaction between periodic replicas. The convergence of k-space sampling was studied and a Monkhorst pack grid of $1 \times 1 \times 6$ was used for the DFT calculations.
The surface was modelled as a periodic slab in a supercell, the results presented in Chapters 6,7 relates to 2×2, and 3×2 supercells for undoped, and H doped surfaces, respectively. A thick vacuum layer ($\sim$15 Å) was included in the direction perpendicular to the surface to ensure no interaction with it's periodic images. Integration over Brillouin zone was performed with k-point sampling mesh of $4 \times 4 \times 1$, and structures were relaxed until forces on all atoms were lower than 0.02 eV/Å. Adsorbates were symmetrically introduced on both top and bottom surfaces to avoid spurious electrostatic interactions between adjacent replicas.
DFT failure to predict band gap was addressed by employing DFT+U only for the relaxed structure, with Hubbard U values of 12.0 eV on Zn 3d orbitals and 6.5 eV on

oxygen 2p orbitals being used, as have been shown to work well for ZnO[80]. Finally, spin polarization was included in calculations involving oxygen molecule.

A.2 Overview of codes

A.2.1 Quantum ESPRESSO

Quantum ESPRESSO [108] is an integrated suite of open-source computer codes for electronic-structure calculations. It features ultrasoft pseudopotentials [185] and the projector augmented plane wave (PAW) method [186]. A number of algorithms which allows implementation of nudged elastic bands method [102, 166] or dimer method [187], ab-initio molecular dynamics [188] amongst others are included in the code.

A.2.2 wanT

The WanT package operates, in principles, as a simple post-processing of any standard electronic structure code. The code allows calculation of Maximally-localized Wannier Functions (WF's), access to spontaneous polarization, density of states, real and complex band structure, and many other properties.The code is available free of charge for researchers in academic environments (http://www.wannier-transport.org).

Bibliography

[1] Afsal Manekkathodi, Ming-Yen Lu, Chun Wen Wang, and Lih-Juann Chen. Direct growth of aligned zinc oxide nanorods on paper substrates for low-cost flexible electronics. *Advanced Materials*, 22(36):4059–4063, 2010.

[2] Hyun-Kyu Park, Keun Young Lee, Ju-Seok Seo, Jin-A Jeong, Han-Ki Kim, Dukhyun Choi, and Sang-Woo Kim. Charge-generating mode control in high-performance transparent flexible piezoelectric nanogenerators. *Advanced Functional Materials*, 21(6):1187–1193, 2011.

[3] Min-Hua Zhao, Zhong-Lin Wang, and Scott X Mao. Piezoelectric characterization of individual zinc oxide nanobelt probed by piezoresponse force microscope. *Nano Letters*, 4(4):587–590, 2004.

[4] Qa Wan, QH Li, YJ Chen, TH Wang, XL He, JP Li, and CL Lin. Fabrication and ethanol sensing characteristics of zno nanowire gas sensors. *Applied Physics Letters*, 84(18):3654–3656, 2004.

[5] M. C. Payne, M. P. Teter, D. C. Allan, T. A. Arias, and J. D. Joannopoulos. *Rev. Mod. Phys.*, 64:1045, 1992.

[6] Paul Erhart, Andreas Klein, and Karsten Albe. First-principles study of the structure and stability of oxygen defects in zinc oxide. *Physical Review B*, 72(8):085213, 2005.

[7] CW Bunn. The lattice-dimensions of zinc oxide. *Proceedings of the Physical Society*, 47(5):835, 1935.

[8] U Ozgur, Ya I Alivov, C Liu, A Teke, MA Reshchikov, S Dogan, VCSJ Avrutin, S-J Cho, and H Morkoc. A comprehensive review of zno materials and devices. *Journal of applied physics*, 98(4):041301–041301, 2005.

[9] Atsushi Tsukazaki, Akira Ohtomo, Takeyoshi Onuma, Makoto Ohtani, Takayuki Makino, Masatomo Sumiya, Keita Ohtani, Shigefusa F Chichibu, Syunrou Fuke, Yusaburou Segawa, et al. Repeated temperature modulation epitaxy for p-type doping and light-emitting diode based on zno. *Nature materials*, 4(1):42–46, 2004.

[10] Kenji Nomura, Hiromichi Ohta, Akihiro Takagi, Toshio Kamiya, Masahiro Hirano, and Hideo Hosono. Room-temperature fabrication of transparent flexible thin-film transistors using amorphous oxide semiconductors. *Nature*, 432(7016):488–492, 2004.

[11] Zheng Wei Pan, Zhong Lin Wang, et al. Nanobelts of semiconducting oxides. *Science*, 291(5510):1947–1949, 2001.

[12] Lionel Vayssieres. Growth of arrayed nanorods and nanowires of zno from aqueous solutions. *Advanced Materials*, 15(5):464–466, 2003.

[13] Zhong Lin Wang. Nanostructures of zinc oxide. *Materials today*, 7(6):26–33, 2004.

[14] Zhong Lin Wang and Jinhui Song. Piezoelectric nanogenerators based on zinc oxide nanowire arrays. *Science*, 312(5771):242–246, 2006.

[15] Horacio D Espinosa, Rodrigo A Bernal, and Majid Minary-Jolandan. A review of mechanical and electromechanical properties of piezoelectric nanowires. *Advanced Materials*, 24(34):4656–4675, 2012.

[16] Ravi Agrawal, Bei Peng, Eleftherios E Gdoutos, and Horacio D Espinosa. Elasticity size effects in zno nanowires- a combined experimental-computational approach. *Nano Letters*, 8(11):3668–3674, 2008.

[17] Andrea Dal Corso, Michel Posternak, Raffaele Resta, and Alfonso Baldereschi. Ab initio study of piezoelectricity and spontaneous polarization in zno. *Physical Review B*, 50(15):10715, 1994.

[18] HJ Xiang, Jinlong Yang, JG Hou, and Qingshi Zhu. Piezoelectricity in zno nanowires: A first-principles study. *Applied physics letters*, 89(22):223111–223111, 2006.

[19] Ravi Agrawal and Horacio D Espinosa. Giant piezoelectric size effects in zinc oxide and gallium nitride nanowires. a first principles investigation. *Nano letters*, 11(2): 786–790, 2011.

[20] A Mitrushchenkov, G Chambaud, J Yvonnet, and QC He. Towards an elastic model of wurtzite aln nanowires. *Nanotechnology*, 21(25):255702, 2010.

[21] Reginald M Penner. Chemical sensing with nanowires. *Annual Review of Analytical Chemistry*, 5:461–485, 2012.

[22] Tetsuro Seiyama, Akio Kato, Kiyoshi Fujiishi, and Masanori Nagatani. A new detector for gaseous components using semiconductive thin films. *Analytical Chemistry*, 34(11):1502–1503, 1962.

[23] Noboru Yamazoe, Go Sakai, and Kengo Shimanoe. Oxide semiconductor gas sensors. *Catalysis Surveys from Asia*, 7(1):63–75, 2003.

[24] QH Li, T Gao, YG Wang, and TH Wang. Adsorption and desorption of oxygen probed from zno nanowire films by photocurrent measurements. *Applied Physics Letters*, 86(12):123117–123117, 2005.

[25] P Feng, Q Wan, and TH Wang. Contact-controlled sensing properties of flowerlike zno nanostructures. *Applied Physics Letters*, 87(21):213111–213111, 2005.

[26] E Comini, G Faglia, G Sberveglieri, Zhengwei Pan, and Zhong L Wang. Stable and highly sensitive gas sensors based on semiconducting oxide nanobelts. *Applied Physics Letters*, 81(10):1869–1871, 2002.

[27] Anderson Janotti and Chris G Van de Walle. Fundamentals of zinc oxide as a semiconductor. *Reports on Progress in Physics*, 72(12):126501, 2009.

[28] Christof Wöll. The chemistry and physics of zinc oxide surfaces. *Progress in surface science*, 82(2):55–120, 2007.

[29] Lukas Schmidt-Mende and Judith L MacManus-Driscoll. Zno–nanostructures, defects, and devices. *Materials today*, 10(5):40–48, 2007.

[30] LS Vlasenko and GD Watkins. Optical detection of electron paramagnetic resonance in room-temperature electron-irradiated zno. *Physical Review B*, 71(12): 125210, 2005.

[31] FA Selim, MH Weber, D Solodovnikov, and KG Lynn. Nature of native defects in zno. *Physical review letters*, 99(8):085502, 2007.

[32] Anderson Janotti and Chris G Van de Walle. Oxygen vacancies in zno. *Applied Physics Letters*, 87(12):122102–122102, 2005.

[33] Woo-Jin Lee, Joongoo Kang, and KJ Chang. Defect properties and p-type doping efficiency in phosphorus-doped zno. *Physical Review B*, 73(2):024117, 2006.

[34] Stephan Lany and Alex Zunger. Dopability, intrinsic conductivity, and nonstoichiometry of transparent conducting oxides. *Physical review letters*, 98(4):045501, 2007.

[35] Chennupati Jagadish and Stephen J Pearton. *Zinc oxide bulk, thin films and nanostructures: processing, properties, and applications*. Elsevier, 2011.

[36] Xudong Wang, Jinhui Song, Jin Liu, and Zhong Lin Wang. Direct-current nanogenerator driven by ultrasonic waves. *Science*, 316(5821):102–105, 2007.

[37] Cheng-Yuan Wang and Sonipon Adhikari. Zno-cnt composite nanotubes as nanoresonators. *Physics Letters A*, 375(22):2171–2175, 2011.

[38] Jun Zhou, Chang Shi Lao, Puxian Gao, Wenjie Mai, William L Hughes, Shao Zhi Deng, Ning Sheng Xu, and Zhong Lin Wang. Nanowire as pico-gram balance at workplace atmosphere. *Solid State Communications*, 139(5):222–226, 2006.

[39] Zuoming Zhu, Tsung-Liang Chen, Yi Gu, John Warren, and Richard M Osgood. Zinc oxide nanowires grown by vapor-phase transport using selected metal catalysts: a comparative study. *Chemistry of materials*, 17(16):4227–4234, 2005.

[40] Won Il Park, D Hl Kim, S-W Jung, and Gyu-Chul Yi. Metalorganic vapor-phase epitaxial growth of vertically well-aligned zno nanorods. *Applied Physics Letters*, 80:4232, 2002.

[41] Brinda B Lakshmi, Charles J Patrissi, and Charles R Martin. Sol-gel template synthesis of semiconductor oxide micro-and nanostructures. *Chemistry of Materials*, 9(11):2544–2550, 1997.

[42] John Conti, Paul Holtberg, et al. International energy outlook 2011. *Washington: Independent Statistics and Analysis of US Energy Information Administration*, 12, 2011.

[43] Min-Yeol Choi, Dukhyun Choi, Mi-Jin Jin, Insoo Kim, Sang-Hyeob Kim, Jae-Young Choi, Sang Yoon Lee, Jong Min Kim, and Sang-Woo Kim. Mechanically powered transparent flexible charge-generating nanodevices with piezoelectric zno nanorods. *Advanced Materials*, 21(21):2185–2189, 2009.

[44] Yong Qin, Xudong Wang, and Zhong Lin Wang. Microfibre–nanowire hybrid structure for energy scavenging. *Nature*, 451(7180):809–813, 2008.

[45] Seung Nam Cha, Ju-Seok Seo, Seong Min Kim, Hyun Jin Kim, Young Jun Park, Sang-Woo Kim, and Jong Min Kim. Sound-driven piezoelectric nanowire-based nanogenerators. *Advanced Materials*, 22(42):4726–4730, 2010.

[46] Guang Zhu, Rusen Yang, Sihong Wang, and Zhong Lin Wang. Flexible high-output nanogenerator based on lateral zno nanowire array. *Nano letters*, 10(8): 3151–3155, 2010.

[47] Raffaele Resta and David Vanderbilt. Theory of polarization: a modern approach. In *Physics of Ferroelectrics*, pages 31–68. Springer, 2007.

[48] K Arshak and I Gaidan. Development of a novel gas sensor based on oxide thick films. *Materials Science and Engineering: B*, 118(1):44–49, 2005.

[49] Harvey E Brown. *Zinc oxide: Properties and applications*. International Lead Zinc Research Organization New York, 1976.

[50] Hans Hartnagel, AL Dawar, AK Jain, and C Jagadish. *Semiconducting transparent thin films*. Institute of Physics Pub. Bristol [England], 1995.

[51] Ghenadii Korotcenkov. Metal oxides for solid-state gas sensors: What determines our choice? *Materials Science and Engineering: B*, 139(1):1–23, 2007.

[52] Noboru Yamazoe. New approaches for improving semiconductor gas sensors. *Sensors and Actuators B: Chemical*, 5(1):7–19, 1991.

[53] Andrei Kolmakov and Martin Moskovits. Chemical sensing and catalysis by one-dimensional metal-oxide nanostructures. *Annu. Rev. Mater. Res.*, 34:151–180, 2004.

[54] E Comini, C Baratto, G Faglia, M Ferroni, A Vomiero, and G Sberveglieri. Quasi-one dimensional metal oxide semiconductors: preparation, characterization and application as chemical sensors. *Progress in Materials Science*, 54(1):1–67, 2009.

[55] Michelle JS Spencer. Gas sensing applications of 1d-nanostructured zinc oxide: Insights from density functional theory calculations. *Progress in Materials Science*, 57(3):437–486, 2012.

[56] Zhong L Wang. Characterizing the structure and properties of individual wire-like nanoentities. *Advanced Materials*, 12(17):1295–1298, 2000.

[57] A Kolmakov. The effect of morphology and surface doping on sensitization of quasi-1d metal oxide nanowire gas sensors. In *Optics East 2006*, pages 63700X–63700X. International Society for Optics and Photonics, 2006.

[58] Matt Law, Hannes Kind, Benjamin Messer, Franklin Kim, and Peidong Yang. Photochemical sensing of no2 with sno2 nanoribbon nanosensors at room temperature. *Angewandte Chemie*, 114(13):2511–2514, 2002.

[59] Zili Zhan, Jianwei Lu, Wenhui Song, Denggao Jiang, and Jiaqiang Xu. Highly selective ethanol in2o3 based gas sensor. *Materials research bulletin*, 42(2):228–235, 2007.

[60] Xu Jiaqiang, Chen Yuping, Li Yadong, and Shen Jianian. Gas sensing properties of zno nanorods prepared by hydrothermal method. *Journal of materials science*, 40(11):2919–2921, 2005.

[61] Ting-Jen Hsueh, Cheng-Liang Hsu, Shoou-Jinn Chang, I Chen, et al. Laterally grown zno nanowire ethanol gas sensors. *Sensors and Actuators B: Chemical*, 126 (2):473–477, 2007.

[62] Jong Yeog Son et al. Horizontal zno nanowires for gas sensor application: Al-doping effect on sensitivity. *Electrochemical and Solid-State Letters*, 12(12):J109–J111, 2009.

[63] M-W Ahn, K-S Park, J-H Heo, J-G Park, D-W Kim, KJ Choi, J-H Lee, and S-H Hong. Gas sensing properties of defect-controlled zno-nanowire gas sensor. *Applied Physics Letters*, 93(26):263103–263103, 2008.

[64] M Breedon, MJS Spencer, and I Yarovsky. Adsorption of no2 on oxygen deficient zno (2110) for gas sensing applications: A dft study. *The Journal of Physical Chemistry C*, 114(39):16603–16610, 2010.

[65] Wei An, Xiaojun Wu, and XC Zeng. Adsorption of o2, h2, co, nh3, and no2 on zno nanotube: a density functional theory study. *The Journal of Physical Chemistry C*, 112(15):5747–5755, 2008.

[66] Michelle JS Spencer and Irene Yarovsky. Zno nanostructures for gas sensing: Interaction of no2, no, o, and n with the zno (1010) surface. *The Journal of Physical Chemistry C*, 114(24):10881–10893, 2010.

[67] JD Prades, A Cirera, and JR Morante. ab initio calculations of no2 and so2 chemisorption onto non-polar zno surfaces. *Sensors and Actuators B: Chemical*, 142(1):179–184, 2009.

[68] P. Hohemberg and W. Kohn. *Phys. Rev.*, 136:864, 1964.

[69] W. Kohn and W. Sham. *Phys. Rev.*, 140:1133, 1965.

[70] E. Fermi. *Rend. Accad. Naz. Lincei*, 6:602, 1927.

[71] L. H. Thomas. *Proc. Cambridge Phil. Roy. Soc.*, 23:542, 1927.

[72] P. A. M. Dirac. *Proc. Cambridge Phil. Roy. Soc.*, 26:376, 1930.

[73] D. M. Ceperley and B. J. Alder. *Phys. Rev. Lett.*, 45:566, 1980.

[74] J. P. Perdew and A. Zunger. *Phys. Rev. B*, 23:5048, 1981.

[75] J. P. Perdew and Y. Wang. *Phys. Rev. B*, 33:8800, 1986.

[76] J. P. Pendew, K. Burke, and M. Ernzerhof. *Phys. Rev. Lett.*, 77:3865, 1996.

[77] Slimane Haffad, Giancarlo Cicero, and Madani Samah. Structural and electronic properties of zno nanowires: a theoretical study. *Energy Procedia*, 10:128–137, 2011.

[78] Giancarlo Cicero, Andrea Ferretti, and Alessandra Catellani. Surface-induced polarity inversion in zno nanowires. *Physical Review B*, 80(20):201304, 2009.

[79] Arrigo Calzolari and Alessandra Catellani. Water adsorption on nonpolar zno (1010) surface: A microscopic understanding. *The Journal of Physical Chemistry C*, 113(7):2896–2902, 2009.

[80] Arrigo Calzolari, Alice Ruini, and Alessandra Catellani. Anchor group versus conjugation: Toward the gap-state engineering of functionalized zno (1010) surface for optoelectronic applications. *Journal of the American Chemical Society*, 133 (15):5893–5899, 2011.

[81] S-H Wei and Alex Zunger. Role of metal d states in ii-vi semiconductors. *Physical Review B*, 37(15):8958, 1988.

[82] Peter Schröer, Peter Krüger, and Johannes Pollmann. First-principles calculation of the electronic structure of the wurtzite semiconductors zno and zns. *Physical Review B*, 47(12):6971, 1993.

[83] John E Jaffe, James A Snyder, Zijing Lin, and Anthony C Hess. Lda and gga calculations for high-pressure phase transitions in zno and mgo. *Physical Review B*, 62(3):1660, 2000.

[84] Dirk Vogel, Peter Krüger, and Johannes Pollmann. Self-interaction and relaxation-corrected pseudopotentials for ii-vi semiconductors. *Physical Review B*, 54(8):5495, 1996.

[85] VI Anisimov, IV Solovyev, MA Korotin, MT Czyżyk, and GA Sawatzky. Density-functional theory and nio photoemission spectra. *Physical Review B*, 48(23):16929, 1993.

[86] H. Hellmann. *Einfuhrung in die Quantumchemie*. Leipzig, 1937.

[87] R. P. Feynmann. *Phys. Rev.*, 56:349, 1939.

[88] Gregory H Wannier. The structure of electronic excitation levels in insulating crystals. *Physical Review*, 52(3):191, 1937.

[89] RD King-Smith and David Vanderbilt. Theory of polarization of crystalline solids. *Physical Review B*, 47(3):1651, 1993.

[90] Raffaele Resta. Macroscopic polarization in crystalline dielectrics: the geometric phase approach. *Reviews of modern physics*, 66(3):899, 1994.

[91] B Sporkmann and H Bross. Calculation of wannier functions for zinc-blende-type semiconductors. *Journal of Physics: Condensed Matter*, 9(26):5593, 1997.

[92] Claudia Sgiarovello, Maria Peressi, and Raffaele Resta. Electron localization in the insulating state: Application to crystalline semiconductors. *Physical Review B*, 64(11):115202, 2001.

[93] Nicola Marzari and David Vanderbilt. Maximally localized generalized wannier functions for composite energy bands. *Physical review B*, 56(20):12847, 1997.

[94] EI Blount. Formalisms of band theory. *Solid State Physics*, 13:305–373, 1962.

[95] D. R. Hamann, M. Schluter, and C. Chiang. *Phys. Rev. Lett.*, 43:1494, 1979.

[96] Kari Laasonen, Roberto Car, Changyol Lee, and David Vanderbilt. Implementation of ultrasoft pseudopotentials in ab initio molecular dynamics. *Physical Review B*, 43(8):6796, 1991.

[97] G Kresse and D Joubert. From ultrasoft pseudopotentials to the projector augmented-wave method. *Physical Review B*, 59(3):1758, 1999.

[98] G Kresse and J Hafner. Norm-conserving and ultrasoft pseudopotentials for first-row and transition elements. *Journal of Physics: Condensed Matter*, 6(40):8245, 1994.

[99] H. J. Monkhorst and J. D. Pack. *Phys. Rev. B*, 13:5188, 1976.

[100] Henry Eyring. The activated complex in chemical reactions. *The Journal of Chemical Physics*, 3:107, 1935.

[101] H. Jónsson, G. Mills, and K. W. Jacobsen. *Nudged elastic band method for finding minimum energy paths of transition*, chapter 16, pages 385–404. World Scientific, 1998.

[102] Graeme Henkelman, Blas P Uberuaga, and Hannes Jónsson. A climbing image nudged elastic band method for finding saddle points and minimum energy paths. *The Journal of Chemical Physics*, 113:9901, 2000.

[103] Leonard J Brillson and Yicheng Lu. Zno schottky barriers and ohmic contacts. *Journal of Applied Physics*, 109(12):121301–121301, 2011.

[104] B Meyer and Dominik Marx. Density-functional study of the structure and stability of zno surfaces. *Physical Review B*, 67(3):035403, 2003.

[105] Walter Water and Sheng-Yuan Chu. Physical and structural properties of zno sputtered films. *Materials Letters*, 55(1):67–72, 2002.

[106] Gregory W Tomlins, Jules L Routbort, and Thomas O Mason. Zinc self-diffusion, electrical properties, and defect structure of undoped, single crystal zinc oxide. *Journal of applied physics*, 87(1):117–123, 2000.

[107] David C Look, Joseph W Hemsky, and JR Sizelove. Residual native shallow donor in zno. *Physical review letters*, 82(12):2552, 1999.

[108] Paolo Giannozzi, Stefano Baroni, Nicola Bonini, Matteo Calandra, Roberto Car, Carlo Cavazzoni, Davide Ceresoli, Guido L Chiarotti, Matteo Cococcioni, Ismaila Dabo, et al. Quantum espresso: a modular and open-source software project for quantum simulations of materials. *Journal of Physics: Condensed Matter*, 21(39): 395502, 2009.

[109] John P Perdew, Kieron Burke, and Matthias Ernzerhof. Generalized gradient approximation made simple. *Physical review letters*, 77(18):3865, 1996.

[110] Hendrik J Monkhorst and James D Pack. Special points for brillouin-zone integrations. *Physical Review B*, 13(12):5188–5192, 1976.

[111] G Carlotti, G Socino, A Petri, and E Verona. Acoustic investigation of the elastic properties of zno films. *Applied physics letters*, 51(23):1889–1891, 1987.

[112] SO Kucheyev, JE Bradby, JS Williams, C Jagadish, and MV Swain. Mechanical deformation of single-crystal zno. *Applied physics letters*, 80(6):956–958, 2002.

[113] Youfan Hu, Yang Liu, Wenliang Li, Min Gao, Xuelei Liang, Quan Li, and Lian-Mao Peng. Observation of a 2d electron gas and the tuning of the electrical conductance of zno nanowires by controllable surface band-bending. *Advanced Functional Materials*, 19(15):2380–2387, 2009.

[114] Hengshan Qiu, Bernd Meyer, Yuemin Wang, and Christof Wöll. Ionization energies of shallow donor states in zno created by reversible formation and depletion of h interstitials. *Physical review letters*, 101(23):236401, 2008.

[115] G Alvin Shi, Michael Stavola, SJ Pearton, M Thieme, EV Lavrov, and J Weber. Hydrogen local modes and shallow donors in zno. *Physical Review B*, 72(19): 195211, 2005.

[116] CH Seager and SM Myers. Quantitative comparisons of dissolved hydrogen density and the electrical and optical properties of zno. *Journal of applied physics*, 94(5): 2888–2894, 2003.

[117] F Herklotz, EV Lavrov, and J Weber. Photoluminescence study of hydrogen donors in zno. *Physica B: Condensed Matter*, 404(22):4349–4353, 2009.

[118] MD McCluskey, SJ Jokela, KK Zhuravlev, PJ Simpson, and KG Lynn. Infrared spectroscopy of hydrogen in zno. *Applied physics letters*, 81(20):3807–3809, 2002.

[119] Chris G Van de Walle. Hydrogen as a cause of doping in zinc oxide. *Physical Review Letters*, 85(5):1012, 2000.

[120] MG Wardle, JP Goss, and PR Briddon. First-principles study of the diffusion of hydrogen in zno. *Physical review letters*, 96(20):205504, 2006.

[121] SJ Jokela and MD McCluskey. Structure and stability of oh donors in zno from high-pressure and infrared spectroscopy. *Physical Review B*, 72(11):113201, 2005.

[122] Lei Wang, Thomas Maxisch, and Gerbrand Ceder. Oxidation energies of transition metal oxides within the gga+ u framework. *Physical Review B*, 73(19):195107, 2006.

[123] HJ Ko, YF Chen, SK Hong, H Wenisch, T Yao, and David C Look. Ga-doped zno films grown on gan templates by plasma-assisted molecular-beam epitaxy. *Applied Physics Letters*, 77(23):3761–3763, 2000.

[124] R Agrawal, O Loh, and HD Espinosa. The evolving role of experimental mechanics in 1-d nanostructure-based device development. *Experimental Mechanics*, 51(1): 1–9, 2011.

[125] MS Majdoub, P Sharma, and T Çağin. Dramatic enhancement in energy harvesting for a narrow range of dimensions in piezoelectric nanostructures. *Physical Review B*, 78(12):121407, 2008.

[126] David A Scrymgeour and Julia WP Hsu. Correlated piezoelectric and electrical properties in individual zno nanorods. *Nano letters*, 8(8):2204–2209, 2008.

[127] Marin Alexe, Stephan Senz, Markus Andreas Schubert, Dietrich Hesse, and Ulrich Gösele. Energy harvesting using nanowires? *Advanced Materials*, 20(21):4021–4026, 2008.

[128] Rodrigo A Bernal, Ravi Agrawal, Bei Peng, Kristine A Bertness, Norman A Sanford, Albert V Davydov, and Horacio D Espinosa. Effect of growth orientation and diameter on the elasticity of gan nanowires. a combined in situ tem and atomistic modeling investigation. *Nano letters*, 11(2):548–555, 2010.

[129] Alexander Mitrushchenkov, Roberto Linguerri, and Gilberte Chambaud. Piezoelectric properties of aln, zno, and hg x zn1- x o nanowires by first-principles calculations. *The Journal of Physical Chemistry C*, 113(17):6883–6886, 2009.

[130] Shuangxing Dai, Mohamed Gharbi, Pradeep Sharma, and Harold S Park. Surface piezoelectricity: Size effects in nanostructures and the emergence of piezoelectricity in non-piezoelectric materials. *Journal of Applied Physics*, 110(10):104305–104305, 2011.

[131] Indrani Dakua and Nitin Afzulpurkar. Piezoelectric energy generation and harvesting at the nano-scale: Materials and devices. 2013.

[132] Dong-Hoon Choi, Chang-Hoon Han, Hyun-Don Kim, and Jun-Bo Yoon. Liquid-based electrostatic energy harvester with high sensitivity to human physical motion. *Smart Materials and Structures*, 20(12):125012, 2011.

[133] M Iwamoto, N Yoda, N Yamazoe, and T Seiyama. role of additives on zno gas sensing. *J. Phys. Chem.*, 80:1989, 1976.

[134] T Seiyama, N Yamazoe, and H Arai. Ceramic humidity sensors. *Sensors and Actuators*, 4:85–96, 1983.

[135] C N Xu, J Tamaki, N Miura, and N Yamazoe. Grain size effects on gas sensitivity of porous sno2 based elements. *Sensors and Actuators B: Chemical*, 3:147, 1991.

[136] Z Zhong, D Wang, Y Cui, M W Bockrath, and C M Lieber. Nanowire crossbar arrays as address decoders for integrated nanosystems. *Science*, 302:1377, 2003.

[137] E F. Patolsky and C. M Lieber. Nanowire nanosensors. *Materials Today*, 8:20–28, 2005.

[138] Y Wu, J Xiang, C Yang, W Lu, and C. M Lieber. Single-crystal metallic nanowires and metal/semiconductor nanowire heterostructures. *Nature*, 430:61–65, 2004.

[139] Y Cui, Q Wei, H Park, and C. M Lieber. Nanowire nanosensors for highly sensitive and selective detection of biological and chemical species. *Science*, 293:1289, 2001.

[140] S Xu, Y Qin, C Xu, Y Wei, R Yang, and Z. L Wang. Self-powerednanowiredevices. *Nature Nanotechnology*, 5:366–373, 20120.

[141] L Tien, H Wang, B Kang, F Ren, P Sadik, D Norton, S Pearton, and J Lin. Room-temperature hydrogen-selective sensing using single pt-coated zno nanowires at microwatt power levels. *Electrochemical and Solid-State Letters*, 8:G230, 2005.

[142] Z L Wang. *Ten years? venturing in ZnO nanostructures: from discovery to scientific understanding and to technology applications.* Chinese Sci Bull, 2009.

[143] Jiaqiang Xu, Jianjun Han, Yuan Zhang, Yu'an Sun, and Bing Xie. Studies on alcohol sensing mechanism of zno based gas sensors. *Sensors and Actuators B: Chemical*, 132(1):334–339, 2008.

[144] Geunjae Kwak and Kijung Yong. Adsorption and reaction of ethanol on zno nanowires. *The Journal of Physical Chemistry C*, 112(8):3036–3041, 2008.

[145] Quanzi Yuan, Ya-Pu Zhao, Limiao Li, and Taihong Wang. Ab initio study of zno-based gas-sensing mechanisms: Surface reconstruction and charge transfer. *The Journal of Physical Chemistry C*, 113(15):6107–6113, 2009.

[146] Vladimir I Anisimov, Jan Zaanen, and Ole K Andersen. Band theory and mott insulators: Hubbard u instead of stoner i. *Physical Review B*, 44(3):943, 1991.

[147] Andrei Kolmakov, Youxiang Zhang, Guosheng Cheng, and Martin Moskovits. Detection of co and o2 using tin oxide nanowire sensors. *Advanced Materials*, 15(12): 997–1000, 2003.

[148] Michelle JS Spencer, Kester WJ Wong, and Irene Yarovsky. Surface defects on zno nanowires: implications for design of sensors. *Journal of Physics: Condensed Matter*, 24(30):305001, 2012.

[149] Xiaoyan Zhou, Jianpeng Li, Ming Ma, and Qingzhong Xue. Effect of ethanol gas on the electrical properties of zno nanorods. *Physica E: Low-dimensional Systems and Nanostructures*, 43(5):1056–1060, 2011.

[150] P Mitra, Ap P Chatterjee, and Himadri Sekhar Maiti. Zno thin film sensor. *Materials Letters*, 35(1):33–38, 1998.

[151] Liwei Wang, Yanfei Kang, Xianghong Liu, Shoumin Zhang, Weiping Huang, and Shurong Wang. Zno nanorod gas sensor for ethanol detection. *Sensors and Actuators B: Chemical*, 162(1):237–243, 2012.

[152] M Lannoo and J Bourgoin. *Semiconductors I: Theoretical Aspects (Berlin: Springer)*. Berlin: Springer, 1983.

[153] Feng Xu, Yuting Shen, Litao Sun, Haibo Zeng, and Yinong Lu. Enhanced photocatalytic activity of hierarchical zno nanoplate-nanowire architecture as environmentally safe and facilely recyclable photocatalyst. *Nanoscale*, 3(12):5020–5025, 2011.

[154] Charlotte Drouilly, Guylene Costentin, Helene Lauron-Pernot, Delphine Bazer-Bachi, Celine Chizallet, and Vincent Lecocq. Method of converting alcohols in the presence of a catalyst of pretreated zinc oxide type, May 6 2011. US Patent App. 13/102,185.

[155] Alan R Allnatt and Alan B Lidiard. *Atomic transport in solids*. Cambridge University Press, 2003.

[156] WJ Moore and EL Williams. Ii. diffusion of zinc and oxygen in zinc oxide. *Discussions of the Faraday Society*, 28:86–93, 1959.

[157] JW Hoffman and I Lauder. Diffusion of oxygen in single crystal zinc oxide. *Trans. Faraday Soc.*, 66:2346–2353, 1970.

[158] R Robin, AR Cooper, and AH Heuer. Application of a nondestructive single-spectrum proton activation technique to study oxygen diffusion in zinc oxide. *Journal of Applied Physics*, 44(8):3770–3777, 1973.

[159] Gregory W Tomlins, Jules L Routbort, and Thomas O Mason. Oxygen diffusion in single-crystal zinc oxide. *Journal of the American Ceramic Society*, 81(4):869–876, 1998.

[160] Hajime Haneda, Isao Sakaguchi, Akio Watanabe, Takamasa Ishigaki, and Junzo Tanaka. Oxygen diffusion in single-and poly-crystalline zinc oxides. *Journal of Electroceramics*, 4(1):41–48, 1999.

[161] Antônio Claret Soares Sabioni, Marcelo José Ferreira Ramos, and Wilmar Barbosa Ferraz. Oxygen diffusion in pure and doped zno. *Materials Research*, 6(2):173–178, 2003.

[162] MG Wardle, JP Goss, and PR Briddon. Theory of li in zno: A limitation for li-based p-type doping. *Physical Review B*, 71(15):155205, 2005.

[163] Fumiyasu Oba, Shigeto R Nishitani, Seiji Isotani, Hirohiko Adachi, and Isao Tanaka. Energetics of native defects in zno. *Journal of applied physics*, 90(2): 824–828, 2001.

[164] AF Kohan, G Ceder, D Morgan, and Chris G Van de Walle. First-principles study of native point defects in zno. *Physical Review B*, 61(22):15019, 2000.

[165] Gustavo M Dalpian and Su-Huai Wei. Photoinduced cation interstitial diffusion in ii–vi semiconductors. *Physical Review B*, 72(7):075208, 2005.

[166] Graeme Henkelman, Gísli Jóhannesson, and Hannes Jónsson. Methods for finding saddle points and minimum energy paths. *Theoretical Methods in Condensed Phase Chemistry*, pages 269–302, 2002.

[167] DB Laks, CG Van de Walle, GF Neumark, PE Blöchl, and ST Pantelides. Native defects and self-compensation in znse. *Physical Review B*, 45(19):10965, 1992.

[168] SB Zhang, S-H Wei, and Alex Zunger. Intrinsic n-type versus p-type doping asymmetry and the defect physics of zno. *Physical Review B*, 63(7):075205, 2001.

[169] Chris G Van de Walle and Jorg Neugebauer. First-principles calculations for defects and impurities: Applications to iii-nitrides. *Journal of Applied Physics*, 95 (8):3851–3879, 2004.

[170] Yanfa Yan, MM Al-Jassim, and Su-Huai Wei. Oxygen-vacancy mediated adsorption and reactions of molecular oxygen on the zno (101 [over^{-}] 0) surface. *Physical Review B*, 72(16):161307, 2005.

[171] Nunzio Roberto D'Amico, Giovanni Cantele, and Domenico Ninno. First-principles calculations of clean and defected zno surfaces. *The Journal of Physical Chemistry C*, 116(40):21391–21400, 2012.

[172] NL Marana, VM Longo, E Longo, JBL Martins, and JR Sambrano. Electronic and structural properties of the (1010) and (1120) zno surfaces. *The Journal of Physical Chemistry A*, 112(38):8958–8963, 2008.

[173] Anderson Janotti and Chris G Van de Walle. Native point defects in zno. *Physical Review B*, 76(16):165202, 2007.

[174] Hugh Stott Taylor. A theory of the catalytic surface. *Proceedings of the Royal Society of London. Series A*, 108(745):105–111, 1925.

[175] Sebastian Polarz, Jennifer Strunk, Vladislav Ischenko, Maurits WE Van den Berg, Olaf Hinrichsen, Martin Muhler, and Matthias Driess. On the role of oxygen defects in the catalytic performance of zinc oxide. *Angewandte Chemie International Edition*, 45(18):2965–2969, 2006.

[176] Adisak Boonchun and Walter RL Lambrecht. Electronic structure of defects and doping in zno: Oxygen vacancy and nitrogen doping. *physica status solidi (b)*, 250 (10):2091–2101, 2013.

[177] R Ferro, JA Rodriguez, and P Bertrand. Peculiarities of nitrogen dioxide detection with sprayed undoped and indium-doped zinc oxide thin films. *Thin Solid Films*, 516(8):2225–2230, 2008.

[178] Keumyoung Seo, Misook Suh, and Sanghyun Ju. Control of oxygen vacancy concentration in zno nanowires containing sulfur as a reducing agent. *Electronic Materials Letters*, 9(3):273–277, 2013.

[179] Edward I Solomon, Paul M Jones, and Jennifer A May. Electronic structures of active sites on metal oxide surfaces: definition of the copper-zinc oxide methanol synthesis catalyst by photoelectron spectroscopy. *Chemical reviews*, 93(8):2623–2644, 1993.

[180] B Meyer and D Marx. First-principles study of co adsorption on zno surfaces. *Journal of Physics: Condensed Matter*, 15(2):L89, 2003.

[181] DK Mishra, J Mohapatra, MK Sharma, R Chattarjee, SK Singh, Shikha Varma, SN Behera, Sanjeev K Nayak, and P Entel. Carbon doped zno: Synthesis, characterization and interpretation. *Journal of Magnetism and Magnetic Materials*, 2012.

[182] Li-Bin Shi, Ming-Biao Li, and Ying Fei. Defect formation and magnetic properties of carbon-doped zno nanowires by the first principles. *Solid State Sciences*, 2012.

[183] JE Stehr, SL Chen, S Filippov, M Devika, N Koteeswara Reddy, CW Tu, WM Chen, and IA Buyanova. Defect properties of zno nanowires revealed from an optically detected magnetic resonance study. *Nanotechnology*, 24(1):015701, 2013.

[184] Andrea Ferretti, Arrigo Calzolari, Benedetta Bonferroni, and Rosa Di Felice. Maximally localized wannier functions constructed from projector-augmented waves or ultrasoft pseudopotentials. *Journal of Physics: Condensed Matter*, 19(3):036215, 2007.

[185] D. Vanderbilt. Soft self-consistent pseudopotentials in a generalized eigenvalue formalism. *Phys. Rev. B.*, 41:7892–7895, 1990.

[186] Peter E Blöchl. Projector augmented-wave method. *Physical Review B*, 50(24): 17953, 1994.

[187] Graeme Henkelman and Hannes Jónsson. A dimer method for finding saddle points on high dimensional potential surfaces using only first derivatives. *The Journal of chemical physics*, 111:7010, 1999.

[188] Richard Car and Mark Parrinello. Unified approach for molecular dynamics and density-functional theory. *Physical review letters*, 55(22):2471, 1985.

Acknowledgements

I wish to thank all the people who assisted me in developing my PhD work: first Giancarlo Cicero and Alessandra Catellani who have been careful supervisors and great mentors to me. I also appreciate friends and colleagues especially those from the Nanowiring network, whose ideas helped in shaping up the research discussion. Special thanks goes to Jane for always being there for me.

This research has been made possible thanks to the fundings from European Union Seventh Framework Programme under grant agreement No. 265073 (ITN-Nanowiring) and hosting by IMEM-CNR, Parma. Most of the calculations were performed in CINECA (IT) through various ISCA projects, IIT(TORINO) and CHPC(CAPETOWN-SA) are gratefully acknowledged for the computing resources.